Permanent magnets segmentation effect on cogging torque of axial flux machines for wind turbines

A Thesis

presented to

the Faculty of Engineering

at Notre Dame University-Louaize

In Partial Fulfillment

of the Requirements for the Degree

Master of Science

by

Nabil Abdel Karim

June 2018

Notre Dame University - Louaize

Faculty of Engineering

Department of Electrical, Computer and Communication Engineering

We hereby approve the thesis of

Nabil Abdel KArim

Candidate for the degree of Master of Science in Electrical and Computer Engineering (MSECE)

Dr. Semaan Georges

_____

Supervisor

Dr. Elias Nassar

_____

Committee Member

Dr. Nassar Mendalek
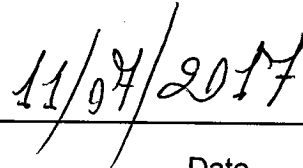
_____

Committee Member

Thesis Release Form

☐ I __Nabil Abdel-Karim__ , authorize Notre Dame University-Louaize to supply copies of my thesis to libraries or individuals on request.

☐ I _____ , do not authorize Notre Dame University-Louaize to supply copies of my thesis to libraries or individuals on request.

_____
Signature

__11/07/2017__
Date

Acknowledgements

This dissertation would not have come into being without the extensive guidance of my supervisors Drs. Semaan Georges, Elias Nassar and Nassar Mendelek. Therefore, I would like to express my deep words of gratitude for their patience, enthusiasm, suggestions, and practical advices. I also thank them for their precious time and their continuous support which have enabled me to carry this work successfully.

Table of Contents

List of Figures

List of Tables

List of Symbols

A	magnetic vector potential
A_g	airgap cross-sectional area
$\boldsymbol{B}_{rem}$	Magnet remanence (normal direction)
$B_{RN(S)}^{(\ell)}$	Magnet remanence for the layer $'\ell'$ (North, South)
$B_\varphi,\ B_z$	flux density components in φz-coordinates
$C_k^{(v)}, D_k^{(v)}, E_k^{(v)}, F_k^{(v)}$	Fourier coefficients of the flux density in region $'v'$
d_s	slot depth
e_{ph}	back-emf per phase
$E_k^{(M,\ell)}, F_k^{(M,\ell)}$	Fourier coefficients of the remanence for a given layer $'\ell'$
E_n^d, F_n^d	Fourier coefficients of the winding distribution function
$f_m^{(I,S)}$	auxiliary function describing the flux density in the armature region
$f(k,n), g(k,n)$	auxiliary functions describing the airgap flux density distribution
J_r	current density vector (radial direction)
N_s	number of slots
N_p	number of pole pairs
$r_o,\ r_i,\ r_m$	outer , inner and mean radius for a given annular slice
$S_k,\ C_k$	auxiliary functions
$\varGamma_{cog}$	cogging torque
φ_s	angular position of slot $'s'$
θ	angle of rotation
$\theta_{mN(S)}^{(\ell)}$	angular span of magnets for the layer $'\ell'$ (North, South)
$\theta_i^{(\ell)}$	angular position of magnets for the layer $'\ell'$
ϕ_g	airgap flux per phase
w_{s0}	slot opening
μ_0	permeability of air
z_i	distance along the normal direction

Abstract

In wind turbine generating systems, Axial Flux Permanent Magnet Synchronous Generators (AFPMSG) are becoming increasingly popular due to many advantages they offer. Nevertheless, these machines suffer from the so-called cogging torque resulting from the interaction between the permanent magnets and the slotted armature. Not only it causes noise and vibration, this cogging torque affects the self-start ability of wind turbines at low wind speed. Therefore, the aerodynamic torque generated by the rotor blades should overcome the cogging torque anytime during the operation otherwise the wind turbine may not come out of stall and never start resulting thus in a loss of electric energy output. Therefore, minimizing its effect is a major design concern for a reliable and smooth operation of small wind turbines. This report presents a new method for reducing cogging torque based on stacking and shifting rotor magnets in the normal direction. First, the exact magnetic field distribution is computed using Maxwell's equations in magnetostatics. This analytical model takes into account the armature slotting effect and the multilayer permanent magnets configuration. Then, the cogging torque is computed by means of Maxwell's stress tensor. The accuracy of the proposed model is validated by finite element analysis. Simulation results show that a substantial peak magnitude reduction can be achieved. Finally, the results of this work are published in the International Journal of Renewable Energy Research (IJRER). This scientific contribution describing the aforementioned model with the corresponding salient points and numerical simulation will appear in Vol.8, 2018.

CHAPTER 1. INTRODUCTION

1.1. World energy mix and investments in renewable energy sectors

For a variety of reasons, demand for electricity is set to grow even further over the next few years. Large markets such as China, India and Brazil are gaining in global importance. More people mean a higher demand for electricity. Worldwide construction is expanding and more and more electrically-powered devices are being used. According to the latest forecasts, demand for electricity will outstrip supply by 2020 [1], resulting in electricity shortages. Industrialization, increasing wealth in emerging markets, globalization and concerns over energy security are also main reasons behind the ever increasing energy demand leading to more pressure on implementing ways to save energy and even more generating electricity from non-conventional fuel based sources namely the renewable ones with a considerable share as shown in figure 1.
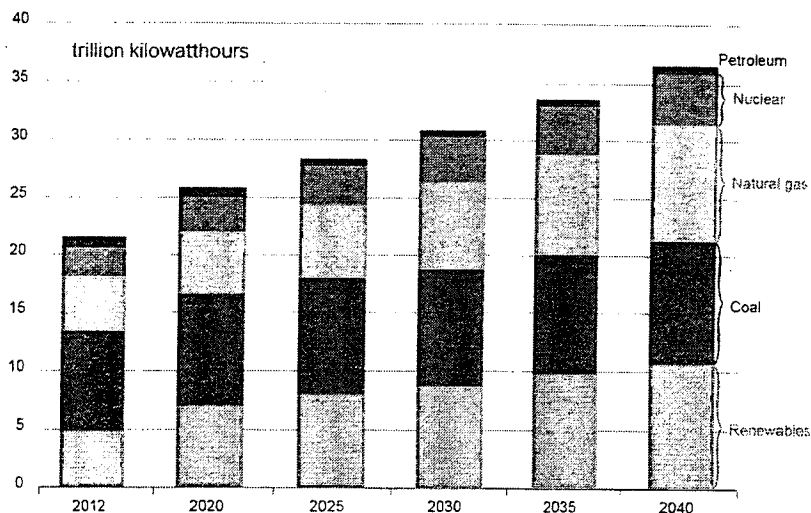
Figure 1, world energy mix by EIA

It is also important to note that coal, natural gas and coal fired power plants will hold the same production level between 2020 and 2040. This is a clear indicator that the demand for electricity for the next few decades will be met be the renewable sources. The world market for renewable energy is booming and accounts for a small but rapidly growing share of total world energy consumption. According to a report by the United Nations Environment program, investment in the renewables sector excluding large hydro power stations is about $241.6bn in 2016 [2].

Crossborder Greenfield investments in renewable energy
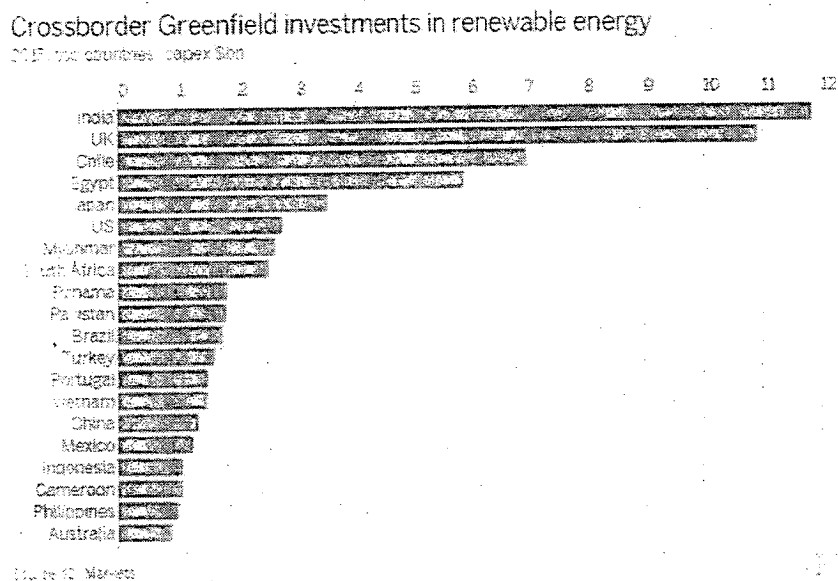
Figure 2, RE investment by country, 2015

This is the case in Chile with huge demand from the mining sector, and India facing the challenges of supplying the huge rural population and satisfying demand due to rapid economic growth. Figure 2 illustrates the global investments in the renewable energy sector for 2015. Surprisingly, emerging countries such as Chile and Egypt come on top of the list.

1.2. Types of renewables & total installed capacity

There are many forms of renewable sources each has its own advantages and drawbacks. Most of them depend in one way or another on sunlight. These include:

- Solar energy;

- Wind power;

- Biomass;

- Geothermal;

- Fuel cells;

- Tidal and ocean energy.

In terms of installed capacity, solar and wind energy dominate other sources by far. As depicted in figure 3, wind power experienced a record year in 2015, with more than 63-GW added – a 22% increase over the 2014 market for a global total of around 433-GW [3].
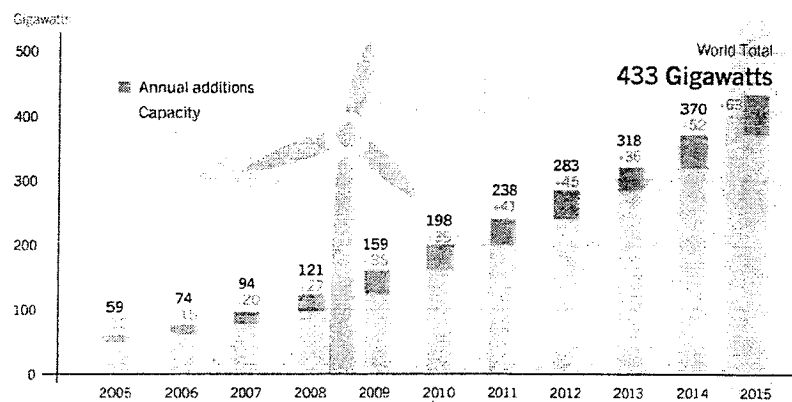
Figure 3, wind power global capacity and annual additions

Other 54-GW are reported to be installed in 2016. It is worthy to note at this point that wind power is successfully competing with other sources with an expected capacity of

792-GW by the end of 2020. China led for new installations, followed by the United States, Germany, Brazil and India as shown in figure 4. Five others in the top 10 were Canada, Poland, France, the United Kingdom and Turkey.
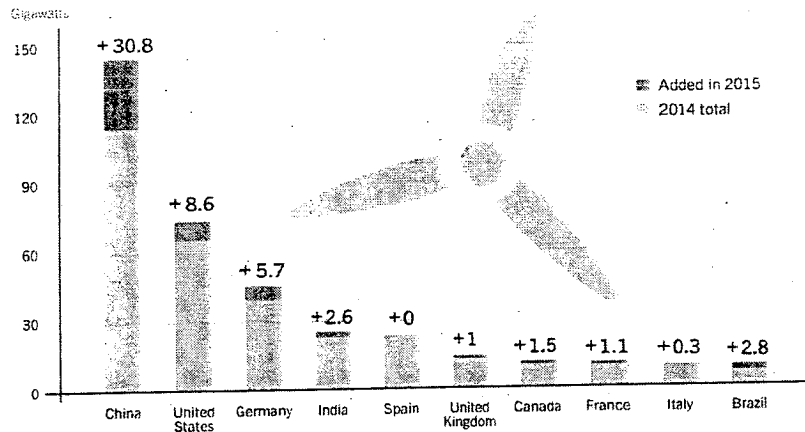
Figure 4. wind power capacity and additions, top 10 countries

The pros and cons of wind energy are subject of heated debate since electricity generated from wind is more expensive than that from conventional sources and the energy output is intermittent because wind is unpredictable and uncontrollable.

As far as solar energy is concerned, the annual new capacity for 2014 is 25% with more than 50-GW added bringing the total global capacity to about 227-GW as shown below.
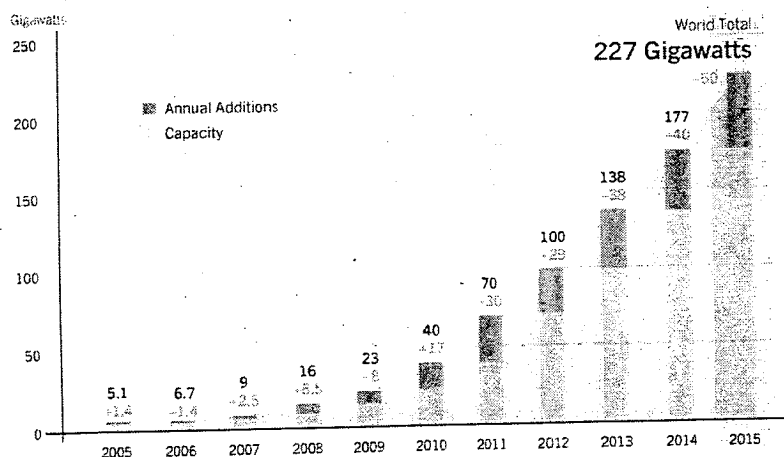
Figure 5. Solar power global capacity and annual additions

The future of solar energy is also bright. Solar industry is expanding dramatically and the annual market was nearly ten times the size of world capacity just a decade ago. The predicted scenario for global capacity for both wind and solar energy is displayed in figure 6 [3].
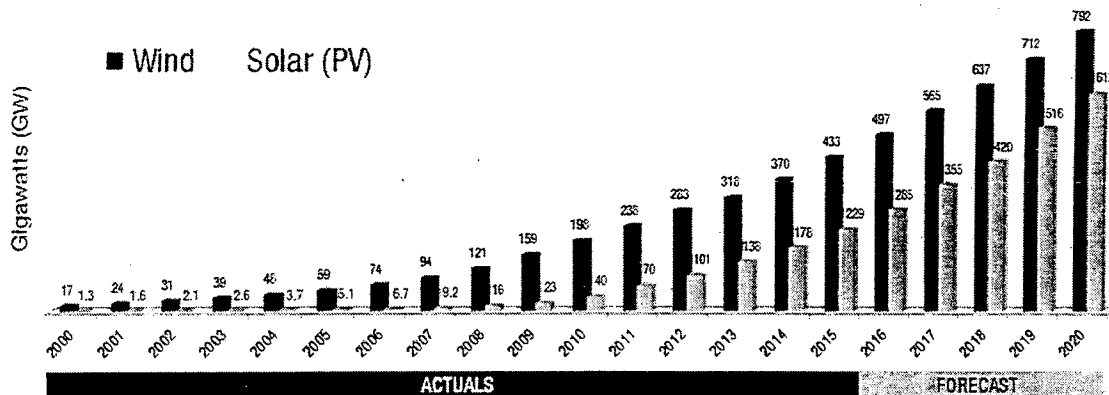
Figure 6, forecast of wind and solar global installed capacity

This info graph shows that solar has lagged significantly behind wind energy in terms of global capacity and annual addition but is gap is being rapidly closing by 2020.

1.3. Principle of operation of a wind turbine

A typical wind turbine is displayed in figure 7 showing the different components for a successful energy conversion. The main objective of these generating systems is to convert the kinetic wind energy sweep by the rotor blades into electrical energy by means of a electromechanical converter followed by a multistage power processor.

Since the wind represents the energy input for such systems, it is useful to start analyzing its behavior and define some important parameters related to this resource. The generators of small turbines often have a significant cogging torque that must be overcome aerodynamically before the blades start turning.
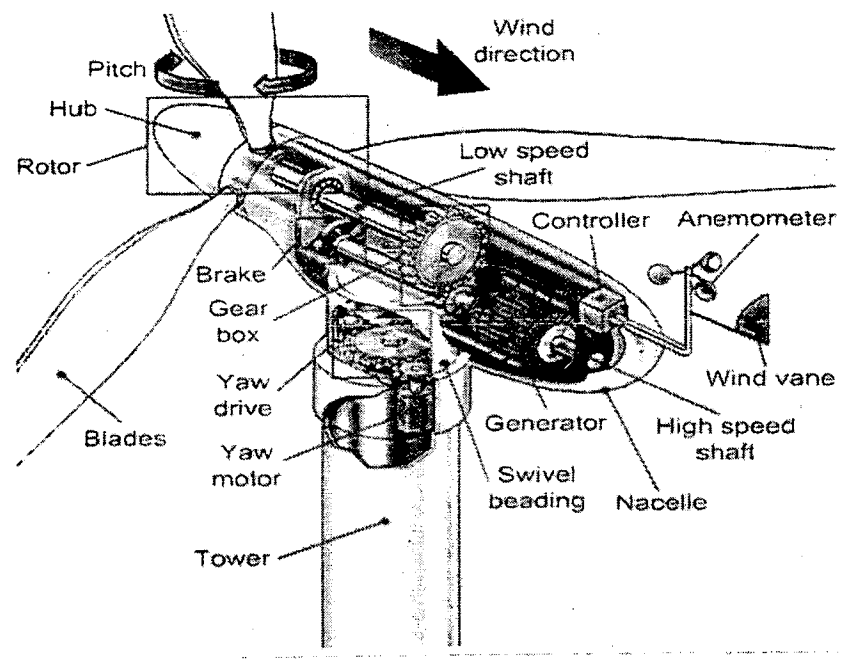
Figure 7, Main components of wind turbine

Most of wind turbines upwind machines, i.e., the blades are in front of the tower when viewed from the wind direction and have three blades. The tail keeps the blades pointing into the wind.

The blades of all wind turbines are comprised of aerofoil sections displayed in figure 8 whose purpose is to produce lift, which is the primary component of the torque about the turbine axis in the direction of blade rotation.
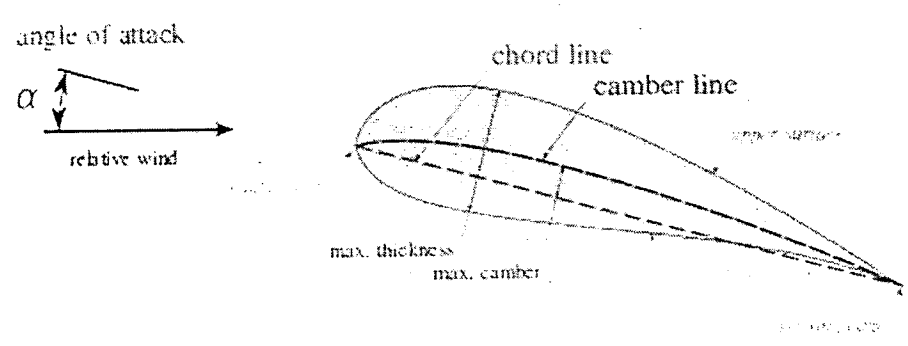
Figure 8: Aerofoil of wind turbine

The product of this torque and the blade angular velocity gives the power extracted from the wind given by:

$$P_{in} = \frac{1}{2} A \rho v_w^3$$

(1.1)

where A, ρ and v_w are the rotor disk area, the air density and the wind speed respectively. Table 1 shows how the wind velocity significantly influences the power available from wind.

Table 1: Output power per unit area
(air density: 1.225 kg/m³)

Wind speed (m/s)	Power/area (W/m²)
0	0
5	77
10	613
15	2,067
20	4,900
25	9,570
30	16,537

To put these numbers into perspective, some typical rotor diameters are shown in figure 9.
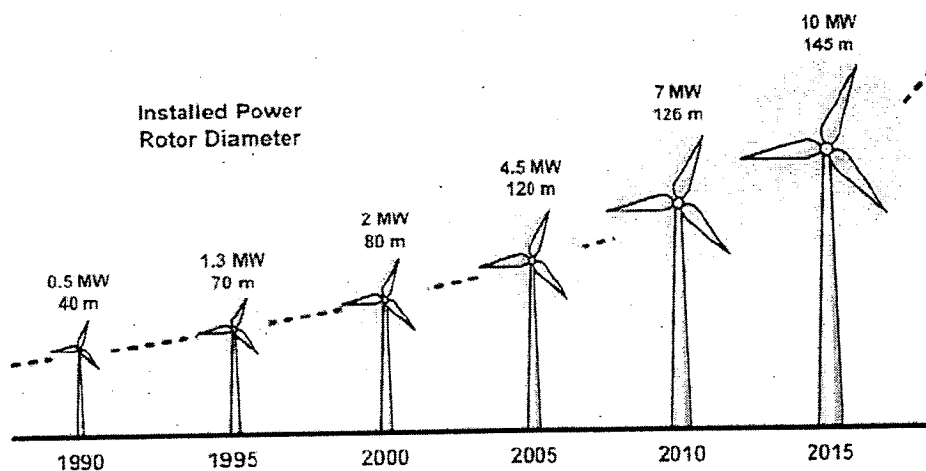
Figure 9. Typical rotor diameter for wind turbines

In general, the blades of a wind turbine are shaped similar to an airplane wing and most of the wind turbines these days are equipped with three blades because they have the highest rotor power coefficient which is an indicator of how much energy can be extracted from the wind by a wind turbine. The power coefficient for different types of wind turbines is shown in figure 10.
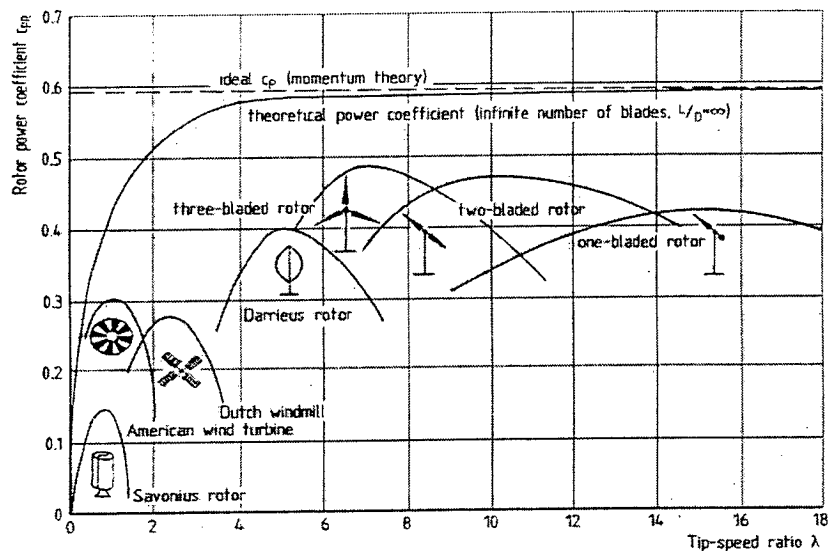
Fig. 10. Impact of number blades on the performance of wind turbine

According to this graph, a three-bladed wind turbine has the ability to extract more power from the wind. The two-blade turbines also have high power coefficient but they are not used in the industry for stability reasons. Moreover, the addition of more blades will not only degrade the energy extraction but also causes excessive tower vibration. It is also important to point out that in theory no wind turbine can extract more that 59% of the total energy available in the wind. This is known as Betz limit and this can be proved by conducting a simple blade element theory analysis.

1.4. Power extracted from wind

In practice, the power delivered by a wind turbine is not linear as shown in figure 11. When the rated wind speed is reached the output power is maintained over a wide range of wind velocity. This is done by adjusting angle of attack of the rotor blades.
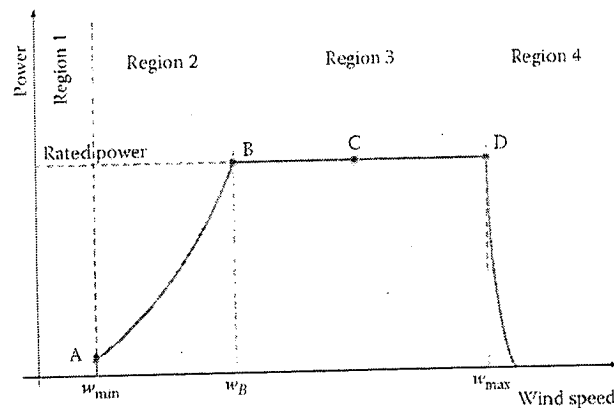
Figure 11. Output power curve for wind turbines

Regardless of the size of the turbine, this graph is characterized by three zones of operation depending on the wind speed.

Table 2: Regions of operation of a wind turbine

Velocity	Description
Cut-in (3-4 m/s)	Energy generation (partial load)
Rated (12-14 m/s)	Rated output power is delivered (full load)
Cut-out (20-25 m/s)	Shut down to prevent mechanical damage

At point A, the wind speed is high enough for energy production. Between A and B, the power output is a cubic function of wind speed as well as the pitch angle. In this region, the pitch angle is adjusted to operate the wind turbine at its maximum Cp to harvest as much energy from the wind as possible. The power at point B is the rated

output power of the turbine. When the wind speed exceeds W_B, the blades are adjusted to spell some of the wind energy to operate the turbine at its rated output.
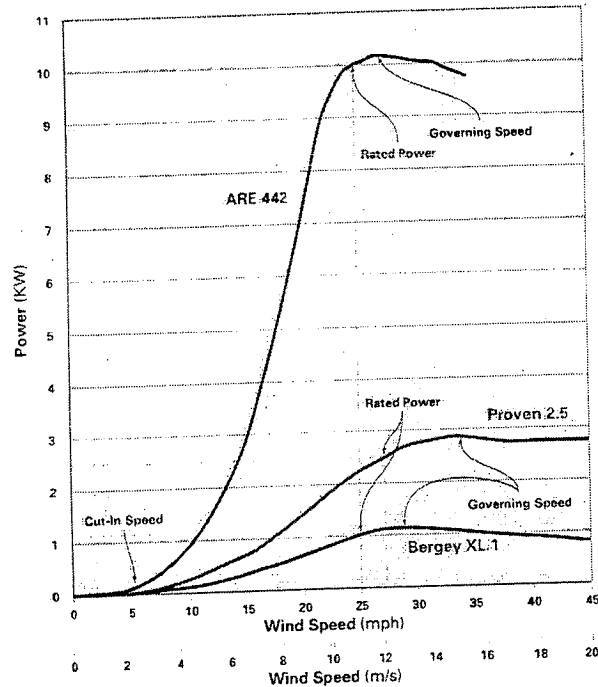
Figure 12. Power curve of real wind turbines

Real power curves for different wind turbines rated at 10, 2.5 and 1-kW are displayed in figure 12. We notice that for the three cases, the rated output is reached at a wind speed of 14 m/s whereas the energy is being delivered for a cut-in wind speed of 5 m/s.

1.5. Rotor Power coefficient

The output performance of a wind turbine is usually characterized by the rotor power coefficient Cp which is the ratio of the power delivered by the rotor blades to the input power swept by the blades. Simply put, it measures the fraction of the power in the wind that is extracted by the rotor. Usually, the rotor blades are equipped with a control mechanism for controlling the power extracted from wind by regulating the

pitch angle β. As shown in figure 13 it is the angle between a plane of rotation and a blade cross-section chord. The impact of the pitch angle is illustrated by the equation below:

$$C_p(\beta, \lambda) = \frac{P_{out}}{\frac{1}{2} A \rho V_w^3} \qquad (1.2)$$

Usually, the rotor power coefficient curve given above is a nonlinear function formulated with two parameters, namely the blade pitch angle β and the tip speed ratio λ:

$$C_p = c_1 \left(c_2 \frac{1}{\lambda_i} - \beta c_3 - c_4 - c_5 \right) e^{-\left(c_6 \frac{1}{\lambda_i} \right)} \qquad (1.3)$$
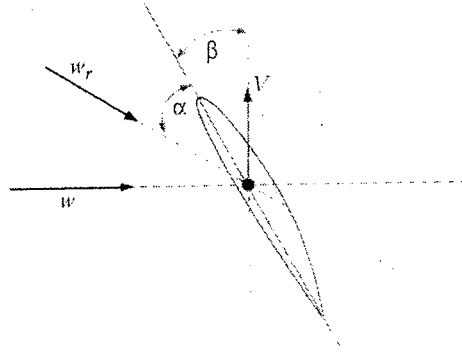
Figure 13. blade pitch angle illustration

In this equation, the tip speed ratio is related to the pitch angle by:

$$\frac{1}{\lambda_i} = \frac{(\lambda + 0.08\beta)(\beta^3 + 1)}{\beta^3 + 1 - 0.035\lambda - 0.0028} \qquad (1.4)$$

Coefficients c1-c6 depends on the design of the turbine rotor blades. According to [4], these following values are tabulated below. It is important to note here that these constants are unique to each wind turbine design and vary from one manufacturer to another.

Table 3: Parameters for the rotor power coefficient computation

c1	0.5	c4	0
c2	116	c5	5
c3	0.4	c6	21

The rotor power coefficient is very important to determine how much power can be extracted from the wind. However, it is difficult to know the precise value of this parameter on a real-time basis because it may change with variations in wind speed and direction. It may also vary from one turbine to another. Usually, the power coefficient curve is provided by the manufacturing as a fixed function or in the form of a look-up table. The variation of the power coefficients versus the tip speed ratio for different value of pitch angles is shown in figure 14. This graph tells us that the maximum power extraction occurs when the pitch angle is zero (no pitch control) for a tip speed ratio $\lambda = 8$, i.e. when the rotational speed of the rotor blades is eight time the wind speed.
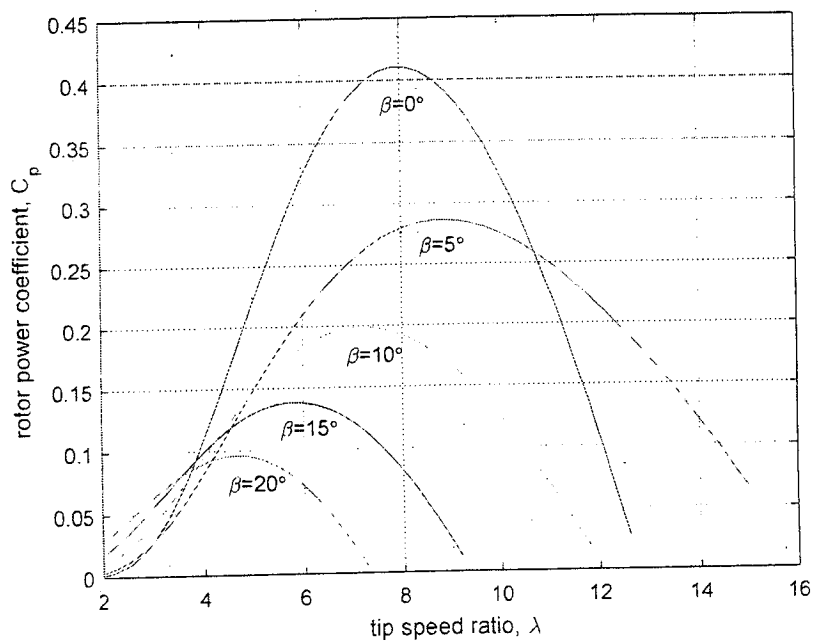
Figure 14. Rotor power coefficient of a real wind turbine

It is also important to note that the true maximum value of C_p do not even get closer to the Betz limit of 59% because this theoretical value derives from a lossless ideal aerodynamic model. This difference is mainly due to various aerodynamic losses.

1.6. Wind resources

Before wind turbines are installed at a given site, measurements of wind speed and direction over a period time are made. Once these data are available and analyzed, the potential for energy production can be assessed. The most suitable function to represent the wind behavior is the Weibull distribution function that represents the probability of distribution for various wind speed. This information is important for siting wind turbines. The Weibull function versus the wind speed w_s has the following form:

$$f(v_w) = \frac{k}{c^k} v_w^{k-1} e^{-\left(\frac{v_w}{c}\right)^k} \tag{1.5}$$

where:

c is the "scale parameter" that can adjust the magnitude of the function.

k is the 'shape parameter" that can shift the peak if the function.

These parameters depend on the geographic location where the wind turbine is installed. Figure 15 shows the dependence of the distribution function for different shape parameters for a yearly basis.
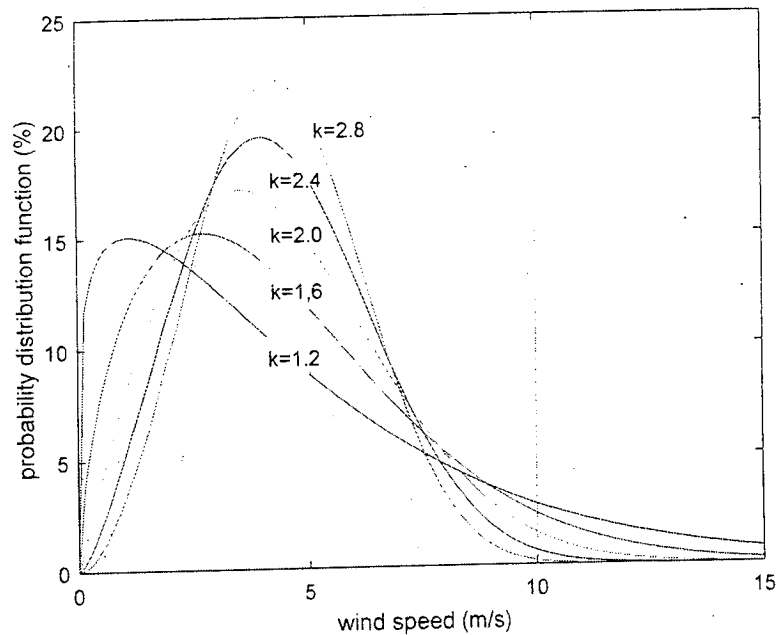
Figure 15, Weibull distribution function for different shape parameters

For instance, if we consider a shape factor of 2.8, the availability of wind speed of 5 m/s or higher is 0.02 x 8760 = 1,752 hr/year. Similar curves can be obtained for different value of the scale parameter.

1.7. Generators for wind turbines

In the early era of the wind energy industry, wind turbines operated at fixed speed. The rotor speed is fixed at a predefined value to match the grid frequency regardless the wind speed. To this end, induction generators with two winding sets or more and an adjustable gear box are used with a soft starter and a capacitor bank for reactive power compensation. During the past decade, variable speed wind turbines become the dominant type among the installed wind turbines worldwide. With variable speed operation, it is possible to adjust the tip speed ratio at a given value to match the maximum rotor power coefficient. This corresponds to the operation at partial load which is represented by the region 2 in figure 10 where the wind speed is

below the rated value and maximum power extraction is guaranteed by controlling the pitch angle β. Variable speed wind energy systems can be equipped with induction and synchronous generators and be connected to the grid through power converters. The disadvantages of such systems are the presence of power converters, the use of more components, the more complex control strategy and the increase cost.

1.7.1. Some aspect about power control

Referring back to figure 10, region 3 is characterized by a constant power output for a wide range of wind speed. To limit that power to a constant level the simplest control method is the *stall control* also known as passive control. Here the blades are bolted to the hub at a fixed angle irrespective the wind speed. This design has a low aerodynamic response and causes the rotor to lose power when the wind speed exceeds a certain level. Another type of control is the *pitch control* known as active control. Here the blades can be turned out or into the wind as the output power becomes too high or too low to assist startup and emergency stop. The third type of control is the *active stall control*. At low wind speed the blades are pitched to extract the maximum amount of energy in the wind. At high wind speed, the blades go into a deeper stall by being pitched into the direction opposite to that of a pitched controlled turbine.

1.7.2. Types of generators

Different types of generators can be used in wind turbine generating systems for the electromechanical conversion. Four main types are commercially available in the market today as depicted in figure 16 and 17 [5].
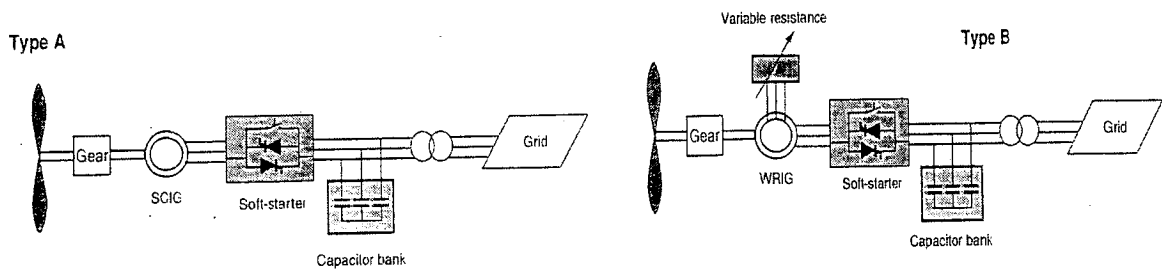
Figure 16. Type A & type B wind generators

SCIG and WRIG stand for squirrel cage induction generator and wound rotor induction generator respectively. Type A configuration denotes the fixed speed wind turbine where the generator is directly connected to the grid via a transformer. Since the SCIG always draws reactive power from the grid, this configuration uses a capacitor bank to compensate the reactive power compensation. A smoother grid connection is achieved by using a soft-starter.

Type B configuration denotes variable speed wind turbine. As shown, it uses a wound rotor induction generator and was firstly introduced in the market by the leader Danish manufacturer Vestas since the mid-1990s. The generator is directly connected to the grid. A capacitor bank performs the reactive power compensation. A smoother grid connection is achieved by using a soft-starter. The total rotor resistance is adjusted by adding extra resistance through slip rings changing thus the slip of the machine. This way, the power output in the system is controlled. The range of the dynamic speed control depends on the size of the variable rotor resistance. Typically, the speed range is 0–10% above synchronous speed. Figure 17 shows the other two generating system types C and D.
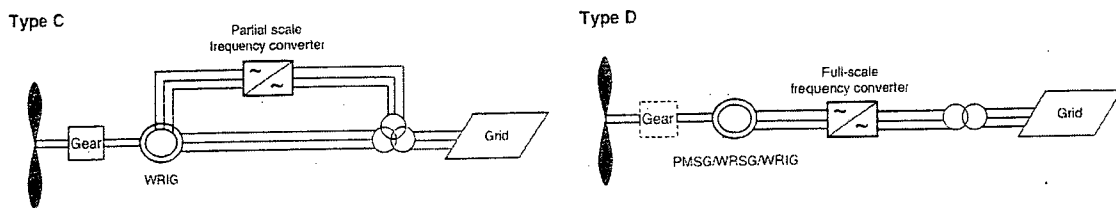
Figure 17. Type C & type D wind generating systems

Type C configuration denotes variable speed wind turbine with doubly fed induction generator and a partial scale frequency converter on the rotor circuitry. The partial scale frequency converter performs the reactive power compensation and the smoother grid connection. Type D corresponds to variable speed with full scale frequency converter. Gearless permanent magnet synchronous generator or induction generator could be used. The synchronous generator can be of conventional radial type or the axial flux type described in the next chapter. The frequency converter performs the reactive power compensation and the smoother grid connection. The table below gives the standard wind turbine types and their control strategy.

Table 4: Wind turbine types

Speed control		Power control		
		Stall	Pitch	Active stall
Fixed speed	Type A	Type A0	Type A1	Type A2
Variable speed	Type B	Type B0	Type B1	Type B2
	Type C	Type C0	Type C1	Type C2
	Type D	Type D0	Type D1	Type D2

The grey zones indicate combination that is not allowed in use in the wind turbine industry today.

1.8. The cogging torque and self-starting ability problem

The design analysis of this study involves the study of cogging torque and its minimization for wind turbines equipped with permanent magnet generators.

Although different types of generators can be used for the electromechanical conversion such as the doubly fed induction generator and wounded rotor induction generator, permanent magnet machines are considered in this study due to many advantages they offer. In this report, axial flux permanent magnet synchronous generators are considered and described in chapter 2. This parasitic cogging torque results from the interaction between the rotor magnets and the slotted armature that must be minimized to reduce noise and vibration. For PM machines, the rotor magnets always tend to align with the stator and move to a position with minimum airgap reluctance preventing thus the generator from starting. If the rotor is moved slightly in either direction, the airgap reluctance increases. This increase in reluctance pushes the magnets back into the alignment position. At low cut-in wind speed (4-5 m/s), the aerodynamic torque generated by the rotor blades should overcome the cogging torque or the turbine may not come out of stall and never start resulting thus in a loss of energy output [6], [7]. For small wind turbine, it was reported that a cogging torque of 1N.m is good enough for a smooth self-start [8]-[9] and for permanent magnet direct-driven generators, its peak value should not exceed 2% of that of the net torque [10]. In its simplest form, the cogging force is related to airgap reluctance $\mathcal{R}$ and the rotor angular position θ by:

$$F_{cog} = -\frac{1}{2}\phi_g^2 \frac{d\mathcal{R}}{d\theta} \qquad (1.6)$$

Based on this equation, the cogging effect is eliminated if either the airgap flux ϕ_g is zero or the variation of the airgap reluctance is zero. Of these two, setting ϕ_g to zero is not possible since this flux must be maximized to produce the desired back-emf. Thus, the cogging effect can be eliminated by making the airgap reluctance constant

with respect to the angular position of the rotor. This is so true for slotless armature which is not the case for most electric machines.

In order to analyze the cogging effect in depth, cogging torque requires the exact prediction of the airgap magnetic field distribution as affected by the slotted armature geometry. Traditionally, the field distribution can be calculated either by numerical or semi analytical methods. Numerical approaches require geometry discretization and meshing prior to the generation of the field solution. These modeling techniques offer many advantages such as handling nonlinear anisotropic materials but they require a great deal of computational time and resources. Therefore, a mesh-free solution is always preferred in the early design stage of electric machines. This report describes the magnetic field distribution and the cogging torque calculation using Fourier analysis where the direct solution of Maxwell's equations in magnetostatics is considered. The cogging torque reduction technique is then carried out by stacking and shifting the rotor magnets in the normal direction.

1.9. International codes and standards regulating the operation of wind turbines

The operation of wind turbines is regulated by international standards pertaining to the design, performance, and power quality. Some of these standards are listed below.

- IEC 61400-1:2005 AMD1:2010 Design requirements;
- IEC 61400-2:2013 Small wind turbines;
- IEC 61400-3:2009 Design requirements for offshore wind turbines;
- IEC 61400-4:2012 Design requirements for wind turbine gearboxes;

- IEC 61400-12-1:2005 Power performance measure'ments of electricity producing wind turbines;

- IEC 61400-13:2015 Measurement of mechanical loads;

- IEC 61400-21:2008 Measurement and assessment of power quality characteristics of grid connected wind turbines;

- IEC 61400-23:2014 Full-scale structural testing of rotor blades;

- IEC 61400-24:2010 Lightning protection;

- IEC 61400-25-1:2006 Communications for monitoring and control of wind power plants - Overall description of principles and models;

- IEC 61400-25-2:2015 Communications for monitoring and control of wind power plants - Information models;

- IEC 61400-25-3:2015 Communications for monitoring and control of wind power plants - Information exchange models;

- IEC 61400-25-4:2008 Communications for monitoring and control of wind power plants - Mapping to communication profile;

- IEC 61400-25-5:2006 Communications for monitoring and control of wind power plants - Conformance testing;

- IEC 61400-25-6:2010 Communications for monitoring and control of wind power plants - Logical node classes and data classes for condition monitoring;

- IEC TS 61400-26-1:2011 Time-based availability for wind turbine generating systems;

- IEC TS 61400-26-2:2014 Production-based availability for wind turbines;

- IEC 61400-27-1:2015 Electrical simulation models - Wind turbines.

1.10. Summary

This chapter provides a brief description to the world energy mix and the types of renewable sources used today for clean energy production. It also covers the principle of operation of wind turbines and looks at relevant topics in wind energy such as wind resources and characteristics. The importance of wind energy industry is emphasized by the rate of annual growth and the worldwide installed capacity. Statistical analysis tools are covered to determine the wind energy potential and estimate the energy output at a given site. This type of analysis relies on the use of the probability density function of wind speed. Moreover, energy extraction from wind and performance of wind turbine are examined and the impact of the rotor blades pitch angle is clearly illustrated. Finally, this chapter looks at the inherent cogging torque developed by the permanent magnet machines and briefly describes how it affects the starting ability of wind turbine generating systems at low cut-in wind speed.

CHAPTER 2. AXIAL FLUX MACHINES: AN

OVERVIEW

2.1. Introduction

Axial Flux Permanent Magnet (AFPM) machines, also called disc type machines, are an attractive solution due to their pancake shape, compact construction and high power density. The main difference between axial flux and radial flux machines is the flux direction that essentially travels parallel to the shaft. AFPM machines are particularly suitable for traction applications, robotics and industrial equipment. Also, their ability to accommodate a large number of poles makes them ideal for low speed applications such as wind turbine generating systems. The most important feature of axial flux machines is that they are modular, i.e., they can have planar and easily adjustable airgaps with slotted, slotless or even ironless armature.

Axial flux machines have distinct advantages over the conventional radial type machine. They can be designed to have a higher torque-to-weight ratio and they are smaller in size and have simple disc shaped rotor and stator structures as depicted in figure 18. This is an important feature of axial flux machines because suitable size and shape to match the space limitation is crucial for some applications such as electric vehicle, wind turbines and space shuttles.
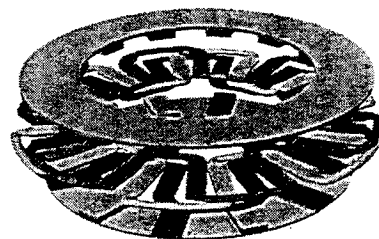
Figure 18. The 3D geometry of axial flux disc type machines

Moreover, the direction of the airgap flux can be changed according to the permanent magnet polarisation and many topologies can be derived.

The history of electric machines reveals that the earliest machines were axial flux machines designed by Faraday in 1831 but shortly after conventional radial flux machines have been widely accepted due the simplicity of their construction.

2.2. Advantages and disadvantages of AFPM

Despite the large variety and construction type of AFPM machines, it is possible to mention some features as advantages and disadvantages with respect to the conventional machines. Some of the advantages are:

- Compact construction and shorter frame;
- High power density;
- No rotor losses (higher efficiency);
- Shorter length in the shaft (axial) direction.

While these points are attractive, these machines suffer from the following:

- Complicated topologies involving two or more airgaps;
- Difficult in automating the manufacturing process for the stator core and windings;
- Deflection of the discs due the important magnetic axial forces;

2.3. Topologies of Axial Flux Machines

From a construction point of view, AFPM machines can be designed as single-sided or double-sided, with or without armature slots, with or without armature core, with internal or external PM rotors, with surface mounted or interior PMs and as multi-stage machines. The diverse topologies of AFPM brushless machines may be classified as follows [11], [12].

2.3.1. Single-sided machine

This is the basic and simplest axial flux structure. The stator consists of a ring type winding embedded in an iron slotted disc. The rotor is formed from iron magnetic materials on which the magnets are embedded as shown in figure 19.
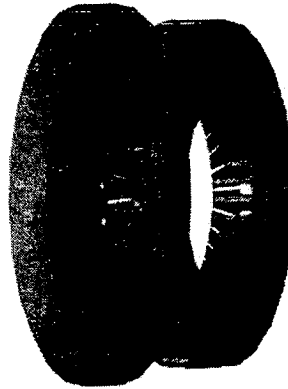
Figure 19. Single-rotor-single-stator AF machine

However, this configuration suffers from large axial forces acting on the stator by the rotor magnets that can twist the discs very easily leading thus to airgap eccentricity problems. These magnetic forces could be attenuated if the stator teeth are removed. It should be noted that the winding facing the rotor magnets are used for torque production or back-emf generations.

2.3.2. Double-rotor, single-stator. The TORUS machines

This type of machines is characterized by double-rotor-single-stator disc structure. The armature configuration can be slotted (TORUS-S) or non-slotted (TORUS-NS). This latter is shown in figure 20.
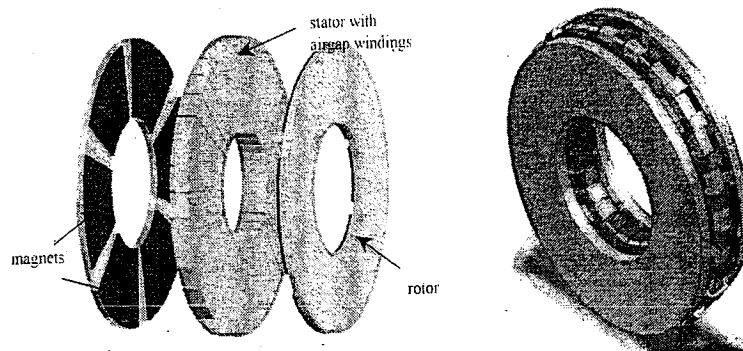
Figure 20. Non-slotted TORUS-NS machine type

This machine has a stator sandwiched between two external rotor discs. The airgap windings are wrapped the stator core with a back-to-back connection. The rotor is formed by arch-shaped surface mounted NdFeB magnets, a rotor core and a shaft. The active conductors are the radial portions of the toroidal winding facing the rotor magnets. The end windings are very short resulting this in less copper, higher efficiency and better heat dissipation. The basic flux path is shown in figure 21.
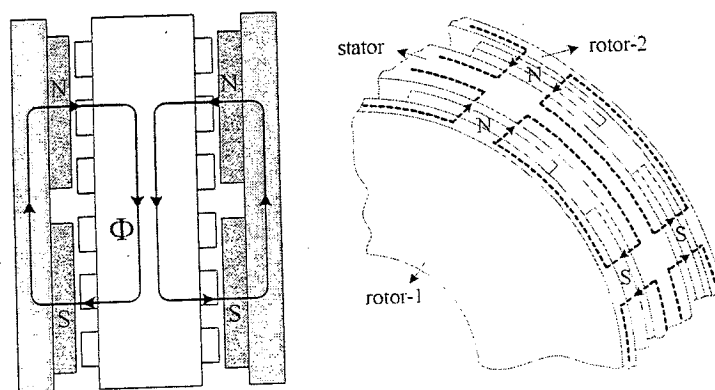
Figure 21. 2D and 3D flux path of the TORUS-NS machine

As can be seen, the magnetic flux leaves the north magnetic pole, crosses the two airgaps into the stator core. Then it takes the circumferential path along the stator core and then enters the rotor core through the opposite pole of the permanent magnets. Therefore, it can be expected a large stator core due the summation if the flux leading causing magnetic saturation. This non-slotted armature provides lower leakage and

mutual inductances. Also, effects resulting from slots such as flux ripple, cogging torque, and tooth saturation are eliminated. The 3D layout of slotted TORUS-S machine is displayed in figure 22.
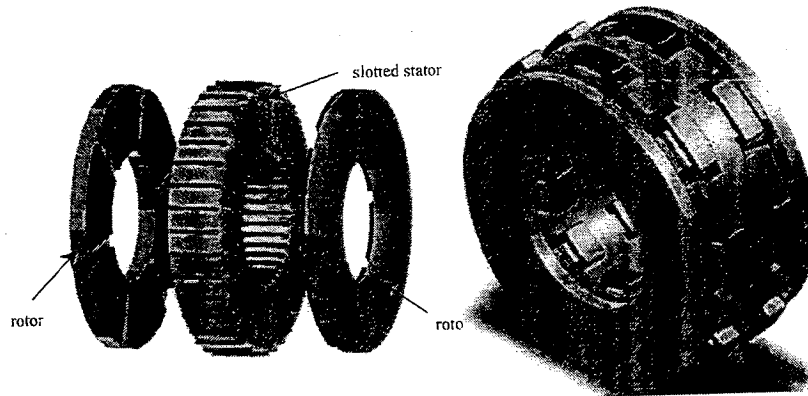
Figure 22, Slotted TORUS-S machine type

This machine has a single stator and two rotors as in the previous structure. Here, the stator has slots with back-to-back connected windings placed into back-to-back slots. The flux path of TORUS-S machine is shown in 23.
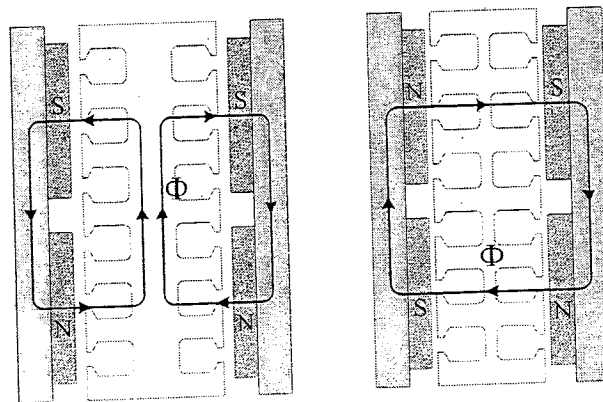
Figure 23, Flux direction for TORUS-S machine, NN and NS type.

For the NN type, the flux travels inside to stator core and closes its path through an opposite permanent magnet whereas for the NS type the flux travels axially ant not circumferentially through stator core. Therefore, the stator yoke is reduced greatly compared to the NN type. This feature leads to less weight, less iron losses, and

higher efficiency. Practically, there is no need for the stator yoke but there must a small one because of the mechanical constraints.

2.3.3. Internal-rotor, external-stator. The AFIR machines

The axial flux internal-rotor (AFIR-NS) machine is illustrated in figure 24. This configuration has two stators and one rotor disc carrying permanent magnets. Distributed back-to-back windings are placed around the stator core. For this topology, no rotor iron discs are used since the main flux does not cross the rotor that is only formed by axially magnetized magnets and a shaft. A nonmagnetic material (Aluminium) is used to fill the gap between magnets to strengthen the structure since ferromagnetic materials are not needed to hold the magnets.

ironless rotor

Non-slotted stator with gramme winding
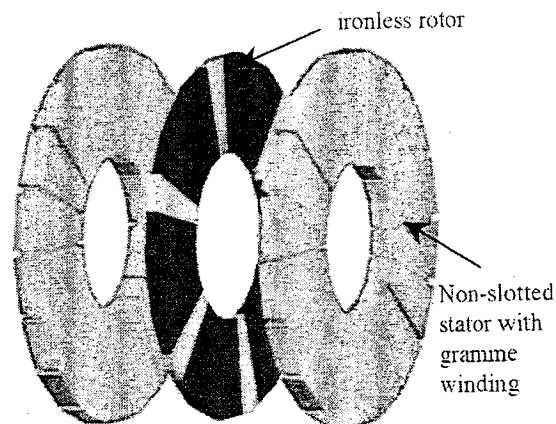
Figure 24. AFIR-NS type machine

This feature makes AFIR machines very attractive for applications which require low inertia. The active winding conductors are located on the inner part of the stator facing the rotor. Therefore the end winding are relatively long resulting in higher copper losses and larger inductance than equivalent TORUS type machines. The flux path is sketched in figure 25.
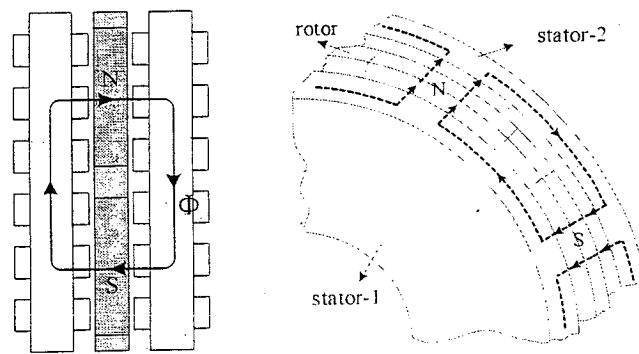
Figure 25, 2D/3D flux lines for AFIR-NS

As it can be seen, the magnetic flux leaves the north pole through the airgap and travels the stator core circumferentially and enters the opposite stator core through the south pole. The slotted AFIR-S is another type of internal rotor disc machines as illustrated in figure 26.
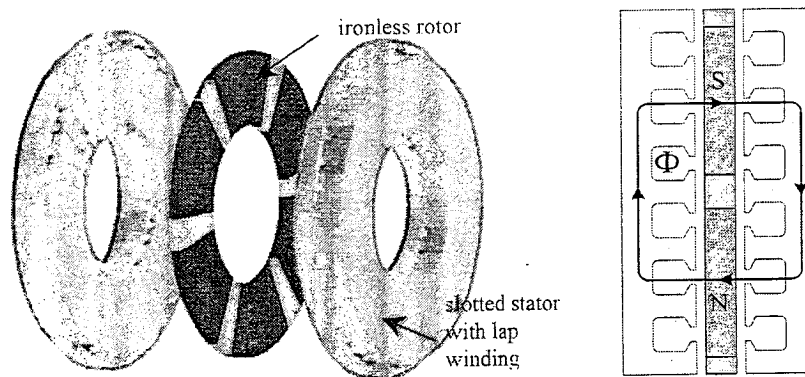
Figure 26, AFIR-S disc type machine and the corresponding flux path

This machine is realized by two stators and one simple rotor formed only by axially magnetized permanent magnets and aluminum to strengthen the structure. The armature lap winding is accommodated in radially carved slots. The basic flux path is the same as in AFIR-NS machine. Again, the flux lines do not travel the rotor core and thus there is no need for magnetic circuit. These machines have short end windings which results in lower copper losses and higher efficiency.

2.3.4. Multi airgap machines

Both TORUS and AFIR type machines and also radial machines can be constructed in multi stage versions. If the machine is required to deliver high torque, a multi disc machine can be used. While these machines have not found enough attention, they are very competitive because of their modularity and easy assembly. They also can achieve higher power densities than the radial multi airgap counterparts. The reason is that the effective airgap area in radial machines gets smaller as going into the inner rotor while the airgap area remains the same for the multi disc slotless (MULTI-NS) axial flux machines as depicted in figure 27.
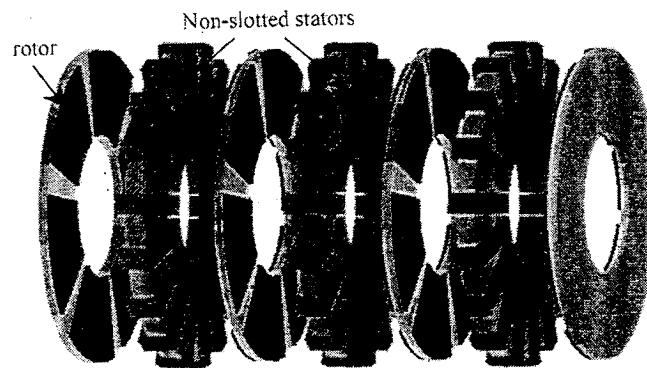
Figure 27. Slotless multi disc machine

Rotors share the same mechanical shaft and rotors with magnetic core are only used for the outer discs to provide the main flux return. They should also be thick enough to resist the magnetic forces and avoid being twisted. The inner rotors are formed by rotor discs with permanent magnet on both sides. The back-to-back winding armature can be connected either in series or parallel. The flux path is basically the same as that for TORUS or AFIR type machines. As can be observed from figure 28, the flux either travels from one outer rotor to the other outer rotor through the N stator, N+ 1

coreless rotor and 2N airgaps (NS type) or travels in each of the rotor and stator

structures (NN types).
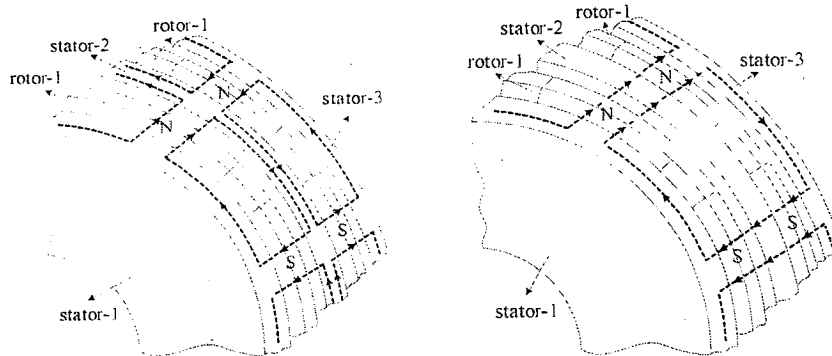
Figure 28, Flux path for NN and NS type multi disc machine

Multi stage machines can also have slotted structure. These MULTI-S machines have

N stator and N+1 rotor like their MULTI-NS counterparts. Again, two different

configurations can be considered, i.e. the NN and the NS type. The multi NN type is

the one in which the magnetic flux travels the stator in the circumferential direction as

shown in figure 29. Therefore, back magnetic iron is needed for each stator.
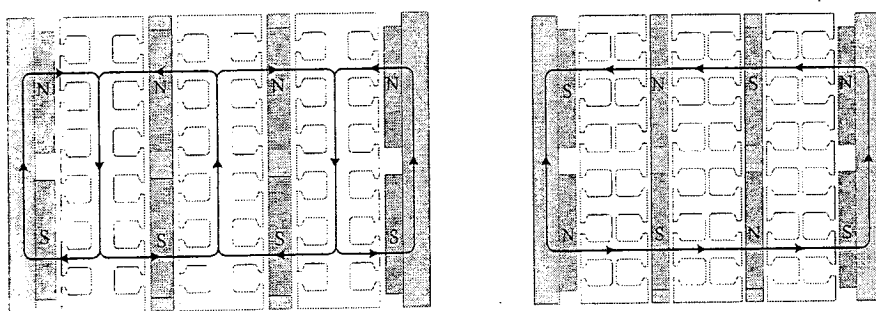
Figure 29: Multi disc machine with slotted armature. NN and NS structures.

The multi NS type is the one in which the magnetic field travels in the axial direction

therefore no stator magnetic circuits (or thin back iron) are involved in this design

resulting thus in a lower weight compared to its NN counterpart. The armature

currents are embedded in teeth distributed and placed in a circular manner along the

stator disc. No materials are wasted since the slots are not carved within the

laminations. On the other hand, the outer rotors required magnetic iron core, the inner ones are made from ironless nonmagnetic materials to increase the robustness of the rotor discs. The advantages of NS type are very apparent. Their size is smaller since no back iron is required resulting in less iron losses and higher power-to-weight ratio.

2.4. Cogging torque in permanent magnet machines

Irrespective of the wind generator topology used for electricity production, these machines will suffer from cogging effect. In fact, the cogging torque may be simply considered as the sum of the interactions of each edge of the permanent magnet with the slot openings. The cogging torque experienced by all stator teeth have the same shape, but are offset from each other in phase by the angular slot pitch. Therefore, the study of cogging torque can be reduced to the analysis of one of these interactions. Figure 30 shows one half of a PM pole and a single slot opening moving with respect to the PM edge. The magnetic energy W_m sum of the air and the PM energy contributions is a function of the angular position ϑ. If the slot opening is in the middle of the PM the variation of with ϑ is null, while it is large if the slot opening is near the PM edge. Moreover, W_m is monotonously decreasing with ϑ; it is possible to verify that the energy in the air gap increases with ϑ, but in the magnet it decreases, and the total energy decreases as well.
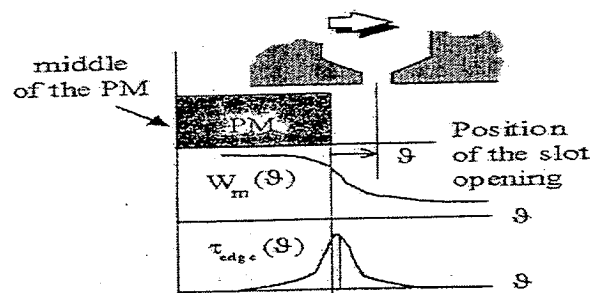
Figure 30. Simple model of cogging torque mechanism

The number of periods of the cogging torque waveform during a rotation of a slot pitch depends on the number of slots and poles. For a rotor with identical PM poles, equally spaced around the rotor, the number of periods during a slot pitch rotation is given by:

$$N_P = \frac{2N_p}{hcf(N_s, 2N_p)} \qquad (2.1)$$

Where N_s and $2N_p$ are the total number of slots and poles respectively, and the denominator is the highest common factor (HCF) between N_s and $2N_p$. It is worth noting here that integral slot machines have greater cogging torque than fractional slot ones. For generators having an integral slot pitch, i.e. $N_s/N_m = q$ (an integer), the first cogging torque harmonic index is q. This represents the worst case situation. On the other hand, for machines having fractional slot pitch where N_s and N_m share no common factor, the first index would then be N_s. This is the best case situation.

2.4.1. Stored energy method

As mentioned previously, cogging torque is caused by the interaction between the PM field and stator slotting which produces noise and vibration. Therefore, motors with closed slots or slotless stator are not affected by cogging torque. In more detail, the cogging torque is caused by the variation of the magnetic energy of the field due to the PM with the angular position of the rotor. Using the traditional method of stored energy and coenergy, the torque can be determined from the generalized forces law:

$$\Gamma_{cog}(\theta) = -\left(\frac{P}{2}\right)\frac{\partial W_{en}}{\partial \theta}\bigg|_{\phi=cst}$$

$$= \left(\frac{P}{2}\right)\frac{\partial W_{coen}}{\partial \theta}\bigg|_{i=cst}$$

(2.2)

The energy stored in the magnetic field is an important quantity to know in the design

of permanent magnet machines. Consider the magnetic circuit below the

instantaneous power delivered to the magnetic field is given by:

$$p = i_1\frac{d\lambda_1}{dt} + i_2\frac{d\lambda_2}{dt}$$

(2.3)
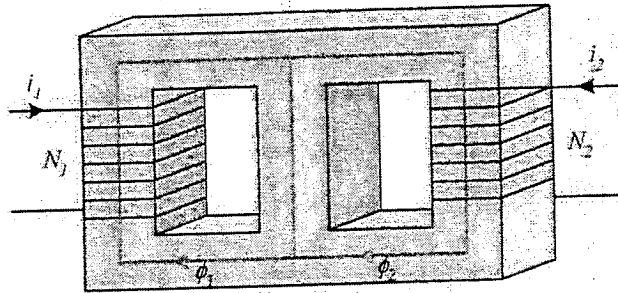
Figure 31. Doubly excited magnetic structure

From this expression, the expression stored in the magnetic field is

$$W = \frac{\lambda_{11}^2}{2L_1} + \frac{\lambda_{22}^2}{2L_2} + \frac{\lambda_{12}\lambda_{21}}{L_{12}}$$

(2.4)

Where $\lambda_{11} = N_1\phi_{11}, \lambda_{22} = N_2\phi_{22}, \lambda_{12} = N_1\phi_{12}$, and $\lambda_{21} = N_2\phi_{21}$. The coenergy

expression is:

$$W_c = \frac{1}{2}L_1 i_1^2 + \frac{1}{2}L_2 i_2^2 + i_1 i_2 L_{12}$$

(2.5)

A comparison between these two equations shows the apparent advantage of using

coenergy is quite obvious. In the presence of permanent magnets, the equation of

coenergy is modified as follows:

$$W_c = \frac{1}{2} L_1 i_1^2 + \frac{1}{2}(R + R_m)\phi_m^2 + Ni\phi_m \qquad (2.6)$$

Where ϕ_m and R are the magnet flux linking the armature winding and the reluctance seen by the magneto motive source respectively. In this expression, the first term is the coenergy stored in the self-inductance, the second term is the coenergy stored due the magnet alone, and the last is the coenergy due the mutual flux.

2.4.2. Fourier series method

Irrespective of whether the cogging torque waveform is determined analytically or by finite-element analysis, it can be described by a Fourier series as follows:

$$\Gamma_{cog}(\theta) = \sum_{k=1}^{\infty} T_k \sin(kN_c\theta + \varphi_k) \qquad (2.6)$$

Where θ represents the rotor angle, T_k and φ_k are the amplitude and the phase angle of the kth harmonic component. N_c is the least common multiple between the number of poles and the number of slots. Furthermore, cogging torque is periodic with respect to each magnet pole since South magnet poles create the same cogging torque as North magnet poles. Minimizing or eliminating cogging torque requires setting all Fourier coefficients to zero or reducing the amplitude of the largest coefficients.

2.5. Some techniques to reduce the cogging torque

In this section, the main techniques for reducing cogging torque will be presented and discussed [13]-[17]. The technique of skewing the stator or the rotor can effectively reduce the torque ripple. However it increases the difficulties in manufacturing the poles and the winding and thus it increases the machine cost. Some

alternative techniques have been proposed to reduce the torque ripple without skewing, even if they may present other disadvantages.

2.5.1. Fractional-slot winding

It can be observed that the torque ripple reduces with fractional-slot windings. However, this technique requires double-layer winding which is not always allowed by automatic winding machines.

2.5.2. Pole arc width

The pole arc width can be arranged to cancel some cogging torque harmonics, generally the fundamental one. However, the exact pole arc width is not easily achievable, since it depends on the PM magnetisation type and on the airgap and slot opening lengths. A reduced pole arc width with respect to the pole pitch improves the back emf waveform as well.

2.5.3. Notches in the stator teeth

Dummy slots can be obtained by introducing in the stator teeth a number of notches. Their effect is to reduce the cogging torque harmonic contents.

$$N_n = 1 \qquad N_n = 2$$
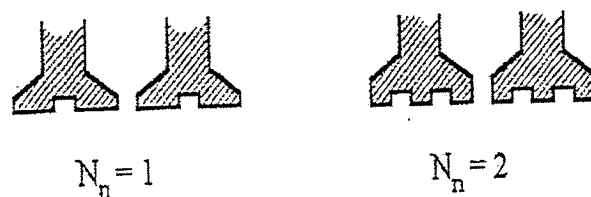
Figure 32. Stator dummy slots

With equally spaced notches in each stator tooth, the harmonics of higher order are cancelled. These notches do not practically influence the back emf but reduces the amplitude and increases the frequency of the cogging torque.

2.5.4. Magnet shifting

Another effective technique to minimise the cogging torque is to displace adjacent magnets relative to each other, as illustrated below.

(a) (b) (c)
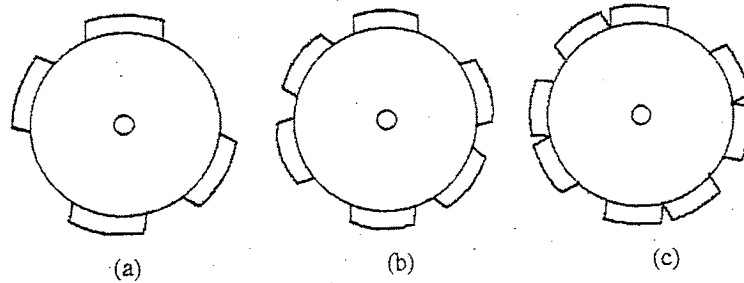
Figure 33, Magnetic shifting

The general rule states that, in a motor with $2p$ poles, the jth pole has to be shifted by an angle:

$$\varphi_j = 2\pi(j-1)/(2pN_pQ) \qquad (2.7)$$

With this method, all cogging torque harmonics are cancelled except those of order multiple of $2p$.

2.6. Axial flux machines operation as wind generators

The main problem when connecting wind turbine generating systems (WTGS) to an existing distribution system is the bus voltage variation. Figure 34 shows a distribution radial feeder operating at a medium voltage where the wind turbine is injecting real power into bus N.

distribution substation
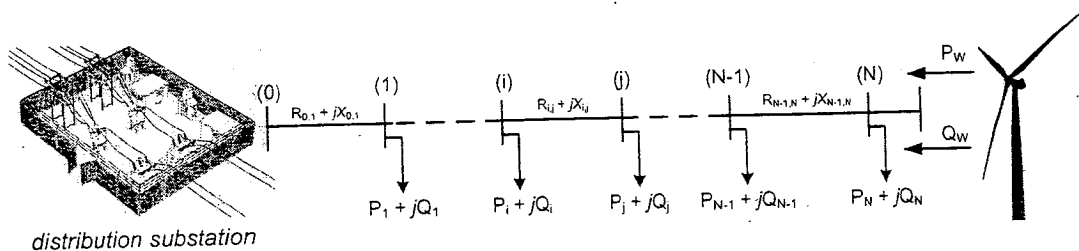
Figure 34. A typical radial distribution network with wind power injection

The complex power at bus j is related to the current I_{ij} flowing in the ij^{th} branch by:

$$S_j^{(j)} = \frac{V_j}{I_{ij}^*} = P_j^{(j)} + jQ_j^{(j)} \tag{2.8}$$

where the power injections are given by:

$$\begin{cases} P_j^{(j)} = P_j + P_{j,j+1}^{(j)} \\ Q_j^{(j)} = Q_j + Q_{j,j+1}^{(j)} \end{cases}$$

The phasor voltage drop in the ij^{th} branch due to the series impedance $Z_{ij} = R_{ij} + jX_{ij}$ and assuming $V_j = V_j e^{j0}$ is equal to:

$$\Delta V_{ij} = Z_{ij} I_{ij} = \frac{P_j^{(j)} R_{ij} + Q_j^{(j)} X_{ij}}{V_j} + j \frac{P_j^{(j)} X_{ij} - Q_j^{(j)} R_{ij}}{V_j} \tag{2.9}$$

Without any loss of generality, the quadrature component of the voltage drop is usually neglected. Hence, the voltage drop becomes:

$$\Delta V_{ij} = \frac{P_j^{(j)} R_{ij} + Q_j^{(j)} X_{ij}}{V_j} \tag{2.10}$$

The right hand side of the expression (2.8) can be extended to account for different branch losses and wind power injection in order to take the following form:

$$S_j^{(j)} = (P_N - P_w) + j(Q_N - Q_W) + \sum_{k=j}^{N-1} (P_k + \Delta P_{k,k+1}) + j(Q_k + \Delta Q_{k,k+1})$$

where $\Delta P_{k,k+1}$ and $\Delta Q_{k,k+1}$ are the active and reactive losses in the branch $(k, k+1)$ respectively. The voltage variation at the bus j as a result of the power injection from the wind turbine is:

$$\delta V_j = \Delta V_{oj} - \Delta V_{0j}^{WTGS} = \frac{P_W \sum_{k=0}^{j-1} R_{k,k+1} + Q_W \sum_{k=0}^{j-1} X_{k,k+1}}{V_n}$$

In this expression it is assumed that all bus voltages are equal to the rated voltage V_n.

In the operation of power network, the bus voltage variation should be less than a

given predefined limit δV_{max}, that is,

$$\delta V_j \leq \delta V_{max}, \quad j \in \{1 \cdots N\}$$

By rearranging the above equations and for a given power factor of the wind turbine,

the output power is determined as follows:

$$P_w \leq \frac{\delta V_{max} \cdot V_n}{\sum_{k=0}^{j-1} R_{k,k+1} + tan(\varphi_w) \sum_{k=0}^{j-1} X_{k,k+1}} \tag{2.11}$$

This equation can be used to determine the rated output power of a wind turbine that

can be connected to a radial network at bus N. Moreover, if the voltage drop at the

point of common coupling (bus N) is set to zero, the reactive power consumed by the

wind turbine should be equal to:

$$Q_W = P_W \frac{\sum_{k=0}^{j-1} R_{k,k+1}}{\sum_{k=0}^{j-1} X_{k,k+1}} = \frac{P_W}{tan(\psi_k)} \tag{2.12}$$

Where ψ_k is the short-circuit impedance angle. Equation (), after multiplying by the

rate voltage and the short-circuit apparent power $S_{kN}^{"}$ at bus N, can take the following

form:

$$\frac{\Delta V_{max}}{V_n} \geq \frac{cP_W}{S_{kN}^{"}} \times \frac{1 - tan(\varphi_w) tan(\psi_k)}{\sqrt{1 + tan^2(\psi_k)}} \tag{2.13}$$

On the other hand, knowing that $S_W^2 = P_W^2 + Q_W^2$, it is possible to express the above

equation as follows:

$$\frac{S_{kN}^{"}}{S_W} \geq \frac{cV_n}{\Delta V_{max}} \times \frac{1 - tan(\varphi_w) tan(\psi_k)}{\sqrt{(1 + tan^2(\varphi_w)) \cdot (1 + tan^2(\psi_k))}} \tag{2.14}$$

The voltage factor c is used in many publications for short-circuit calculation. For distribution systems, it is estimated between 1 and 1.1.

The equation above relates the apparent power ratio to the short-circuit impedance angle $tan(\psi_k)$ for different values of wind turbine power factor $tan(\varphi_w)$ and the voltage drop limit ΔV_{max}.

2.7. Benefits from connecting WTGS and consumer requirements

The main role of distribution networks is to deliver electric energy to the consumers in *ready-to-use* form. That is, the voltage should be within an acceptable range and free of large fluctuations, high level of harmonics, or transient disturbances. Moreover, the electric service must be reliable so an uninterrupted power flow is secured. Reliable delivery means delivering all of the power demanded all of the time and regardless of the use of WTGS, the distribution substation remains the ultimate source of energy at least for the foreseeable future but adding distributed generations (solar or wind generating sources) will help support an existing distribution network in the following points as tabulated below.

Table 5: Benefit of WTGS connected to an existing distribution system

Cover the utility's service territory, reaching all consumers who wish to be connected and purchase power especially in rural areas.
The distribution system will have sufficient capability to meet the peak of those energy.
Satisfactory continuity of service (reliability) to the connected energy consumers.
Stable voltage quality regardless of load level or conditions.

Regardless of the utilization voltage of each country, the delivery system involving renewables must maintain the voltage provided to each customer within a narrow range centred within the range that electric equipment is designed to tolerate and any fluctuation must occur slowly. Such stable voltage profile can be sometimes difficult to obtain due to the variability of the wind speed and direction (or solar irradiance). These goals are to be met and above all else, they need to be achieved at the lowest possible cost and in a safe and aesthetically acceptable manner. From the consumer's perspective, three main requirements can be defined:

- **Voltage level at the connection point of the consumer.** The voltage level has to remain an acceptable range and in a *ready-to-use* form for a reliable operation.

- **Power availability on demand.** The electric power should be available all the time without any interruption whether delivered from thermal power plant or renewable sources.

- **Economic power supply.** The energy should be sold at a reasonable cost. The first two requirements concern the reliability of power supply. Greater reliability means higher costs and hence a conflict will arise for the demand of electricity at an affordable price.

2.8. Network integration issues for wind power

The connection of wind generators to an existing power network influences largely the system state and stability, the power flows, the bus voltages, and the power losses. The factors are largely affected by the following points:

- Location of the wind turbine in the distribution system. The point of common coupling (PCC) influences the power quality. As a rule of thumb, the consumers closer to the PCC are more affected than others.

- The bus voltage variation. This change mainly results from wind velocity but other factors such cogging torque and switching the wind turbine also play an important role. Flicker which occurs at the consumer side is also a result from voltage variation. These variations are attributed to real and reactive power flow after connecting the wind turbine.

- Harmonics injection resulting from the power electronics converters. The effect of harmonics can lead to serious power quality degradation, increase of losses, and overload of compensation devices.

- Short-circuit currents. The connection of wind turbines increases the short-circuit current level. For wind generator equipped with induction machines, these current are quickly damped.

- Stability of the network. Voltage stability, steady-state stability and dynamic stability can be considered.

- Real power losses that usually changes after the connection of WTGS. The increase or decrease level depends on the PCC and the amount of power injected by the wind turbine.

2.9. Summary

This chapter has provided an overview of different types of axial flux permanent magnet synchronous machines for wind generation. It also presents an overview on the infamous cogging torque and describes some techniques to minimize

its impact. This chapter also looks at the benefits that will accrue from the integration of wind turbines into an existing electric distribution system. Equations for determining the size of wind turbines based on the maximum allowable voltage drop are derived. Finally, some technical constraints arising from connecting wind generating systems are discussed.

CHAPTER 3.

EXACT 2D MAGNETIC MODELING OF

WIND GENERATORS

3.1. Introduction

In this chapter an analytical model to compute the exact magnetic field distribution for surface mounted permanent machines is presented in details. The magnetic field analysis in PM machines is an important prerequisite for the prediction of different torque components, axial forces acting on the discs, inductances and so on. Magnet configuration, magnetization direction, airgap length, and the number of the pole and slot combination have significant effects on the airgap flux density. Further, the presence of armature slots has a large influence on the field distribution and consequently on the generator's performance in terms of cogging torque causing noise and vibration and speed fluctuations. Slotting affects the magnetic field in two ways. First, it reduces the total flux per pole. Second, it affects the distribution of the airgap flux density. Therefore, the slotting effect is an important consideration during determination of the airgap flux density. Cogging torque requires the exact computation of the airgap magnetic field as affected by the slotted armature geometry [18]-[20]. Traditionally, the field distribution can be calculated either by numerical or semi analytical methods. However, numerical methods require geometry discretization and meshing prior to the generation of the field solution. These modeling techniques offer many advantages such as handling nonlinear anisotropic materials but they require a great deal of computational time and resources. Therefore,

a mesh-free solution is always preferred in the early design stage of electric machines. This chapter describes the magnetic field distribution and the cogging torque calculation using Fourier analysis where the direct solution of Maxwell's equations in magnetostatics is considered [21]-[23]. The cogging torque reduction technique is carried out by stacking and shifting the rotor magnets in the normal direction. With this configuration, the cogging torque magnitude is greatly reduced to an acceptable level with little effect on the back-emf.

3.2. Generator geometry and assumptions

The 3D inherent geometry of an interior stator axial flux permanent magnet synchronous generator is shown in figure 34. During this analysis, the radial dependency of the magnetic field is neglected. This implies that the field solution is two-dimensional and it is carried out using polar coordinates. This is a valid assumption since the radial component will not greatly impact the magnetic field solution. Using FEA it was shown that the field radial component is zero at the machine's mean radius and gains some negligible amplitude as we move radially toward the machine's edges [24].
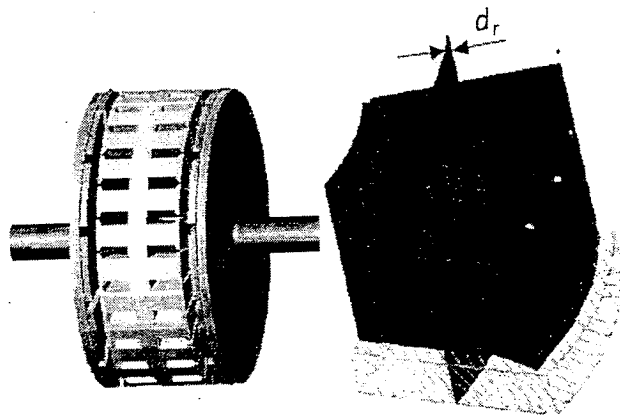
Figure 35: The 3D inherent geometry of Axial Flux Machines

In order to improve the computation of the secondary parameters such as torque and back-emf, the machine is subdivided into N_{sl} radial annular slices and the magnetic vector potential solution is carried out for each slice d_r. The different design parameters affecting the field solution are shown in figure 35. The rotor is equipped with multi-layer surface mounted permanent magnets. Layer one is made up of magnets 1 and 1' and so forth. In this study, each magnetic pole is composed of three magnet pieces shifted by an angle $\theta_i^{(\ell)}$ and each layer 'ℓ' is characterized by the magnets remanence $B_{RN(S)}^{(\ell)}$, their angular span $\theta_{mN(S)}^{(\ell)}$, and their relative angular position $\theta_i^{(\ell)}$ with respect to the interpolar axis. All magnets are shifted by a given amount so that they all fit within a pole pitch. In order to obtain the 2D analytical solution, the following assumptions are made:

- the magnetic materials are linear, homogenous and infinitely permeable;

- the rotor magnets operates on the recoil line with a unity relative permeability and are magnetized in the normal direction;

- the end effects are neglected and open armature slots with parallel sides are considered.
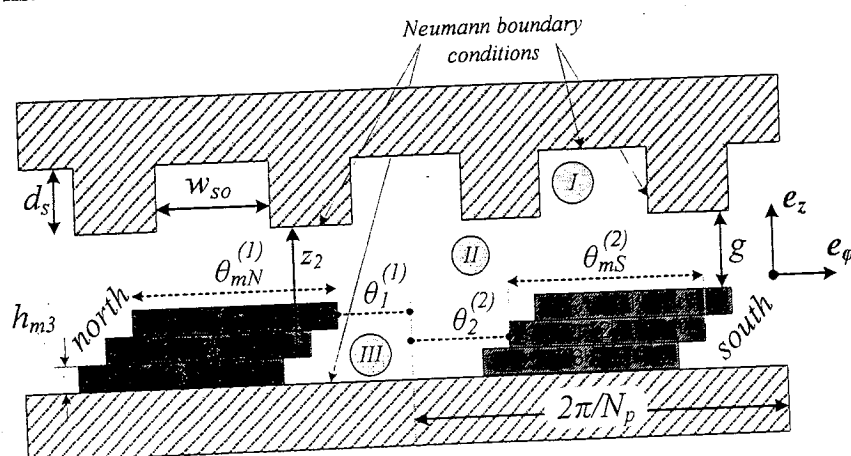
Figure 36: 2D cutting plane at the mean radius

Since the magnetic materials are highly permeable, the magnetic field distribution is not calculated inside the soft-magnetic materials but Neumann conditions apply at their edges in order to predict the field distribution. To do so, the machine is divided into three regions, namely the current-carrying region (the slots), the source-free region (the airgap), and the magnetized region. For each region, Neumann boundary conditions, continuous boundary conditions or a combination of both are considered. Neumann conditions appear at the interface of the magnetic materials and the boundary conditions in the normal direction give rise to a set of linear algebraic system whose unknowns are the flux density coefficients.

3.3. Open-circuit field solution

The field solution is based on the magnetic potential vector A which is a convenient way to find the flux density B in each region of the machine. For magnetostatics problems, combining Maxwell's equations give rise to the well-known Poisson's equation:

$$\nabla^2 A = -\mu J_r - \nabla \times B_{rem} \tag{3.1}$$

where J_r and B_{rem} are the current density vector and the remanence magnetization vector respectively. Written in polar coordinates equation (1) takes the following form:

$$\frac{1}{r_m^2}\frac{\partial^2 A_r}{\partial \varphi^2} + \frac{\partial^2 A_r}{\partial z^2} = -\left(\mu_0 J_r + \frac{1}{r_m}\frac{\partial B_R}{\partial \varphi}\right) \tag{3.2}$$

This partial differential form reduces to Laplace equation in the source-free region. Equation (2) has to be solved in different domains of the machine and this is done for each annular slice at the corresponding mean radius r_m. Moreover, since the cogging

torque computation only requires the field produced by the magnets, the current density J_r is set to zero in (3.2).

Since the flux density vector is given by $\boldsymbol{B} = \nabla \times \boldsymbol{A}$, the field components are related to the magnetic vector potential by:

$$B_\varphi = \frac{\partial A_r}{\partial z}; \; B_z = \frac{1}{r}\frac{\partial A_r}{\partial \varphi} \qquad (3.3)$$

Using the separation of variables technique, the magnetic vector potential for a given region 'v' is given by:

$$A_r^{(v)} = a_0^{(v)} + \sum_{k \neq 0} \frac{r_m}{k\lambda} \left(C_k^{(v)} \operatorname{ch}\left(\frac{k\lambda z}{r_m}\right) + D_k^{(v)} \operatorname{sh}\left(\frac{k\lambda z}{r_m}\right) \right) \cdot \left(E_k^{(v)} \cos(k\lambda\varphi) + F_k^{(v)} \sin(k\lambda\varphi) \right) \qquad (3.4)$$

where $\lambda = \gcd(Ns, Np)$ and $v = I, II$ and III is used for region indexing. Ns and Np denote the total number of slots and the number of magnet pole pairs respectively. For symmetric non-fractional slot machines, λ is usually equal to Np. In the following subsections, field components are derived for each region by taking into account Neumann conditions and continuous boundary conditions at the interface of each domain [25].

3.3.1. Slots area (region-I)

This domain is made up of Ns/Np slots. For each slot, Neumann boundary conditions occur at the sides of the windable slot depth and at the bottom interface adjacent to the stator yoke as shown in figure 35. In this region, the current density and the magnetization vectors are zero reducing thus Poisson's equation to Laplace equation expressed as:

$$\frac{1}{r_m^2}\frac{\partial^2 A_r}{\partial\varphi^2} + \frac{\partial^2 A_r}{\partial z^2} = 0 \tag{3.5}$$

The Fourier expression of the field components in this region are:

$$B_\varphi^{(I,S)} = \sum_{m\neq 0} f_m^{(I,S)} \frac{sh\left(\dfrac{m\pi(z+d_s)}{r_m w_{so}}\right)}{ch\left(\dfrac{m\pi d_s}{r_m w_{so}}\right)} cos\left(\frac{m\pi}{r_m w_{so}}(\varphi - \varphi_s)\right) \tag{3.6}$$

$$B_z^{(I,S)} = \sum_{m\neq 0} f_m^{(I,S)} \frac{ch\left(\dfrac{m\pi(z+d_s)}{r_m w_{so}}\right)}{ch\left(\dfrac{m\pi d_s}{r_m w_{so}}\right)} sin\left(\frac{m\pi}{r_m w_{so}}(\varphi - \varphi_s)\right) \tag{3.7}$$

The angular position of the slot 's' is defined by as $\varphi_s =$

3.3.2. Airgap field solution (region II)

In this source-free region, the tangential and normal components of the flux density are described respectively by Fourier series as:

$$B_\varphi^{(II)} = \sum_{k\neq 0} \begin{array}{c}\left(E_k^{(II)} sh(kN_p z r_m^{-1}) + F_k^{(II)} ch(kN_p z r_m^{-1})\right) sin(k\lambda\varphi) \\ + \\ \left(C_k^{(II)} sh(kN_p z r_m^{-1}) + D_k^{(II)} ch(kN_p z r_m^{-1})\right) cos(k\lambda\varphi)\end{array} \tag{3.8}$$

$$B_z^{(II)} = \sum_{k\neq 0} \begin{array}{c}\left(C_k^{(II)} ch(kN_p z r_m^{-1}) + D_k^{(II)} sh(kN_p z r_m^{-1})\right) sin(k\lambda\varphi) \\ - \\ \left(E_k^{(II)} ch(kN_p z r_m^{-1}) + F_k^{(II)} sh(kN_p z r_m^{-1})\right) cos(k\lambda\varphi)\end{array} \tag{3.9}$$

The continuous boundary conditions to be met for the airgap and the top layer of the magnetized region are given in (9).

$$\begin{cases} B_{z|_{z=-g}}^{(II)} = B_{z|_{z=-g}}^{(III,1)} \\ B_{\varphi|_{z=-g}}^{(II)} = B_{\varphi|_{z=-g}}^{(III,1)} \end{cases} \tag{3.10}$$

The development of (3.10) gives the relation between the airgap field coefficients and those of the magnetized region as follows:

$$
\begin{cases}
C_k^{(II)} = C_k^{(III,1)} + F_k^{(M,1)} ch\left(kN_p g r_m^{-1}\right) \\
D_k^{(II)} = D_k^{(III,1)} - F_k^{(M,1)} sh\left(kN_p g r_m^{-1}\right) \\
E_k^{(II)} = E_k^{(III,1)} - E_k^{(M,1)} ch\left(kN_p g r_m^{-1}\right) \\
F_k^{(II)} = F_k^{(III,1)} + E_k^{(M,1)} sh\left(kN_p g r_m^{-1}\right)
\end{cases}
\tag{3.11}
$$

Subscript *'III, i'* refers to the layer *'i'* in the magnetized region *III*. These coefficients are obtained by applying the boundary conditions in the normal direction between the different regions.

3.3.3. Permanent magnets domain (region III)

It is assumed that the magnets are normally magnetized and are invariant in the normal direction. The remanence function is written as:

$$
B_R^{(\ell)}(\varphi) = \sum_{k \neq 0} E_k^{(M,\ell)} \cos\left(kN_p \varphi\right) + F_k^{(M,\ell)} \sin\left(N_p \varphi\right)
\tag{3.12}
$$

The nth harmonic Fourier coefficients in (3.11) for a given layer *'ℓ'* are given by:

$$
E_k^{(M,\ell)} = \frac{-1^{(k)}}{k\pi}
\begin{cases}
B_{RN}^{(\ell)}\left(\sin kN_p\left(\theta_1^{(\ell)} + \theta_{mN}^{(\ell)} - \theta_0\right) - \sin kN_p\left(\theta_1^{(\ell)} - \theta_0\right)\right) \\
- \\
B_{RS}^{(\ell)}\left(\sin kN_p\left(\theta_2^{(\ell)} + \theta_{mS}^{(\ell)} + \theta_0\right) - \sin kN_p\left(\theta_2^{(\ell)} + \theta_0\right)\right)
\end{cases}
\tag{3.13}
$$

$$
F_k^{(M,\ell)} = \frac{-1^{(k)}}{k\pi}
\begin{cases}
B_{RN}^{(\ell)}\left(\cos kN_p\left(\theta_1^{(\ell)} + \theta_{mN}^{(\ell)} - \theta_0\right) - \cos kN_p\left(\theta_1^{(\ell)} - \theta_0\right)\right) \\
+ \\
B_{RS}^{(\ell)}\left(\cos kN_p\left(\theta_2^{(\ell)} + \theta_{mS}^{(\ell)} + \theta_0\right) - \cos kN_p\left(\theta_2^{(\ell)} + \theta_0\right)\right)
\end{cases}
\tag{3.14}
$$

$B_{RN}^{(\ell)}$ and $B_{RS}^{(\ell)}$ are the north and south induction remanence for the layer *'ℓ'* and θ_0 denotes the angle of rotation. Since the source terms are expressed as Fourier series, then each term creates like harmonic term in the flux density expression. Therefore, the expression of the field components becomes:

$$B_\varphi^{(III,i)} = \sum_{k \neq 0} \begin{array}{c} \left(E_k^{(III,i)} \, \text{sh}\left(kN_p z r_m^{-1}\right) + F_k^{(III,i)} \, \text{ch}\left(kN_p z r_m^{-1}\right) \right) \sin\left(kN_p\varphi\right) \\ + \\ \left(C_k^{(III,i)} \, \text{sh}\left(kN_p z r_m^{-1}\right) + D_k^{(III,i)} \, \text{ch}\left(kN_p z r_m^{-1}\right) \right) \cos\left(kN_p\varphi\right) \end{array} \quad (3.15)$$

$$B_z^{(III,i)}$$

$$= \sum_{k \neq 0} \begin{array}{c} \left(C_k^{(III,i)} \, \text{ch}\left(kN_p z r_m^{-1}\right) + D_k^{(III,i)} \, \text{sh}\left(kN_p z r_m^{-1}\right) + F_k^{(M,i)} \right) \sin\left(kN_p\varphi\right) \\ - \\ \left(E_k^{(III,i)} \, \text{ch}\left(kN_p z r_m^{-1}\right) + F_k^{(III,i)} \, \text{sh}\left(kN_p z r_m^{-1}\right) - E_k^{(M,i)} \right) \cos\left(kN_p\varphi\right) \end{array} \quad (3.16)$$

For this region, Neumann boundary conditions in the normal direction are satisfied at the rotor yoke surface leading to:

$$\begin{cases} D_k^{(III,3)} = -C_k^{(III,3)} T_{kN_p}(z_3) \\ F_k^{(III,3)} = -E_k^{(III,3)} T_{kN_p}(z_3) \end{cases} \quad (3.17)$$

substituting (3.16) in (3.15) gives:

$$B_\varphi^{(III,3)} = \sum_{k \neq 0} \begin{array}{c} \left(E_k^{(III,3)} \sin\left(kN_p\varphi\right) + C_k^{(III,3)} \cos\left(kN_p\varphi\right) \right) \cdot \\ \left(\text{sh}\left(kN_p z r_m^{-1}\right) - T_{k\lambda}(z_3) \, \text{ch}\left(kN_p z r_m^{-1}\right) \right) \end{array} \quad (3.18)$$

$$B_z^{(III,3)}$$

$$= \sum_{k \neq 0} \begin{array}{c} \left(C_k^{(III,3)} \left(\text{ch}\left(kN_p z r_m^{-1}\right) - T_{kN_p}(z_3) \, \text{sh}\left(kN_p z r_m^{-1}\right) \right) + F_k^{(M,i)} \right) \sin\left(kN_p\varphi\right) \\ - \\ \left(E_k^{(III,3)} \left(\text{ch}\left(kN_p z r_m^{-1}\right) - T_{k\lambda}(z_3) \, \text{sh}\left(kN_p z r_m^{-1}\right) \right) - E_k^{(M,i)} \right) \cos\left(kN_p\varphi\right) \end{array}$$

$$(3.19)$$

Equations (3.18) and (3.19) are the starting point for the computation of the magnetic field distribution in different regions of the machine from which the field of different regions can be computed. Moreover, the boundary conditions between different layers of the magnetized region lead to the following set of equations describing the relationship between the field coefficients of the different layers as follows:

$$C_k^{(III,1)} = C_k^{(III,3)} + \sum_{i=1}^{N_\ell - 1} \left(F_k^{(M,i+1)} - F_k^{(M,i)} \right) ch\left(k N_p z_i r_m^{-1} \right)$$

$$D_k^{(III,1)} = D_k^{(III,3)} + \sum_{i=1}^{N_\ell - 1} \left(F_k^{(M,i)} - F_k^{(M,i+1)} \right) sh\left(k N_p z_i r_m^{-1} \right)$$

(3.20)

$$E_k^{(III,1)} = E_k^{(III,3)} + \sum_{i=1}^{N_\ell - 1} \left(E_k^{(M,i)} - E_k^{(M,i+1)} \right) ch\left(k N_p z_i r_m^{-1} \right)$$

$$F_k^{(III,1)} = F_k^{(III,3)} + \sum_{i=1}^{N_\ell - 1} \left(E_k^{(M,i+1)} - E_k^{(M,i)} \right) sh\left(k N_p z_i r_m^{-1} \right)$$

and

$$\begin{cases} C_k^{(III,2)} = C_k^{(III,3)} + \left(F_k^{(M,3)} - F_k^{(M,2)} \right) ch\left(k N_p z_2 r_m^{-1} \right) \\ D_k^{(III,2)} = D_k^{(III,3)} + \left(F_k^{(M,2)} - F_k^{(M,3)} \right) sh\left(k N_p z_2 r_m^{-1} \right) \\ E_k^{(III,2)} = E_k^{(III,3)} + \left(E_k^{(M,2)} - E_k^{(M,3)} \right) ch\left(k N_p z_2 r_m^{-1} \right) \\ F_k^{(III,2)} = F_k^{(III,3)} + \left(E_k^{(M,3)} - E_k^{(M,2)} \right) sh\left(k N_p z_2 r_m^{-1} \right) \end{cases}$$

(3.21)

Here $z_{i(=1,2,3)}$ is the distance in the normal direction measured between the interface of the airgap/teeth and the bottom of the magnet that belongs to the layer $'\ell'$ as depicted in figure 36. It is important to note at this point that if aligned magnets are considered (without any shifting), the coefficients $E_k^{(M,1)}$, $E_k^{(M,2)}$ and $E_k^{(M,3)}$ are all identical and $E_k^{(III,1)} = E_k^{(III,2)} = E_k^{(III,3)}$. This is the equivalent to the case of rotors with single magnetic poles.

3.3.4. Derivation of Fourier coefficients for the Magnetized region

A combination of Neumann and boundary conditions occurs at the interface between region I and region II. The boundary conditions apply between the airgap and the slot openings. For a given slot $'s'$ $(\varphi_s \leq \varphi \leq \varphi_s + w_s)$:

$$\begin{cases} B_{z|z=0}^{(s)} = B_{z|z=0}^{(II)} \\ B_{\varphi|z=0}^{(s)} = B_{\varphi|z=0}^{(II)} \end{cases} \tag{3.22}$$

Additional boundary conditions between the airgap and the magnetic regions adjacent

to it $(\varphi_s + w_s \le \varphi \le \varphi_{s+1})$ are: $B_{\varphi|z=0}^{(s)} = 0$ (Neumann conditions).

The following system of linear equations follows from the application of equation

(3.22).

$$T_{k\lambda}(z_3)C_k^{(III,3)} + \sum_{n \ne 0} (g(k,n) - f(k,n))C_n^{(III,3)} =$$

$$-F_k^{(M,1)}S_{k,01} - F_k^{(M,2)}S_{k,12} - F_k^{(M,3)}S_{k,20} \tag{3.23}$$
$$- \sum_{n \ne 0} \frac{\left(F_n^{(M,1)}C_{n,01} + F_n^{(M,2)}C_{n,12} + F_n^{(M,3)}C_{n,2\frac{j\pi}{2}} \right)}{(g(k,n) - f(k,n))}$$

$$T_{k\lambda}(z_3)E_k^{(III,3)} + \sum_{n \ne 0} (g(k,n) + f(k,n))E_n^{(III,3)} =$$

$$E_k^{(M,1)}S_{k,01} + E_k^{(M,2)}S_{k,12} + E_k^{(M,3)}S_{k,20} \tag{3.24}$$
$$+ \sum_{n \ne 0} \frac{\left(E_n^{(M,1)}C_{n,01} + E_n^{(M,2)}C_{n,12} + E_n^{(M,3)}C_{n,2\frac{j\pi}{2}} \right)}{(g(k,n) + f(k,n))}$$

auxiliary functions C_k and S_k are defined as follows:

$$S_{k,ab} = \text{sh}\big(kN_p/r_m z_a\big) - \text{sh}\big(kN_p/r_m z_b\big)$$

$$C_{k,ab} = \text{ch}\big(kN_p/r_m z_a\big) - \text{ch}\big(kN_p/r_m z_b\big)$$

Functions f and g are only defined when $k \pm n$ are multiple of Ns/Np giving rise to

large sparse matrices represented by sparse data structures proportional to the nonzero

entries. Their corresponding expressions are:

$$f(k,n) = \sum_{m \ne 0} \frac{\big(2mkN_sN_pw_{so}^2\big)T_{\frac{m\pi}{w_{so}}}\big(\frac{d_s}{r_m}\big)\delta_m\big(\frac{-n}{2}N_pw_{so}, \frac{k}{2}N_pw_{so}\big)}{\big((m\pi)^2 - (kN_pw_{so})^2\big)\big((m\pi)^2 - (nN_pw_{so})^2\big)}$$

$$g(k,n) = \sum_{m \neq 0} \frac{\left(2mkN_sN_pw_{so}^2\right)T_{\frac{m\pi}{w_{so}}}\left(\frac{d_s}{r_m}\right)\delta_m\left(\frac{n}{2}N_pw_{so}, \frac{k}{2}N_pw_{so}\right)}{\left((m\pi)^2 - \left(kN_pw_{so}\right)^2\right)\left((m\pi)^2 - \left(nN_pw_{so}\right)^2\right)}$$

With sparse programming, computing higher harmonic orders for the magnetic field is possible without leading to ill-conditioned matrices. For the airgap magnetic field computation, considering the first 128 harmonics usually gives satisfactory results. In this context, sparsity techniques in MATLAB were used and substantial savings in terms of both computational time and resources have been made. The sparse matrix form for (3.23) and (3.24) is:

$$C_k^{(III,3)} = -\left(T_{\lambda p}(z_3)H\right)^{-1}\begin{bmatrix} \left(S_{k,01} + C_{k,01}H\right)F_k^{(M,1)} + \\ \left(S_{k,12} + C_{k,12}H\right)F_k^{(M,2)} + \\ \left(S_{k,20} + C_{k,2\frac{j\pi}{2}}H\right)F_k^{(M,3)} \end{bmatrix} \qquad (3.25)$$

and

$$E_k^{(III,3)} = +\left(T_{\lambda p}(z_3)L\right)^{-1}\begin{bmatrix} \left(S_{k,01} + C_{k,01}L\right)E_k^{(M,1)} + \\ \left(S_{k,12} + C_{k,12}L\right)E_k^{(M,2)} + \\ \left(S_{k,20} + C_{k,2\frac{j\pi}{2}}L\right)E_k^{(M,3)} \end{bmatrix} \qquad (3.26)$$

S and T are diagonal matrices of order k, C is a square matrix made up of identical rows, $H(i, j) = g(i, j) - f(i, j)$ and $L(i, j) = g(i, j) + f(i, j)$. Solving the linear system of equations (3.25) and (3.26) gives the exact solution of the magnetic field in the sub-region *(III, 3)*.

3.4. Analytical results

Figure 37 shows the magnetic field distribution versus the rotor angle in the airgap region at no-load condition for a symmetric slotted permanent magnet machine with no magnet shifting.
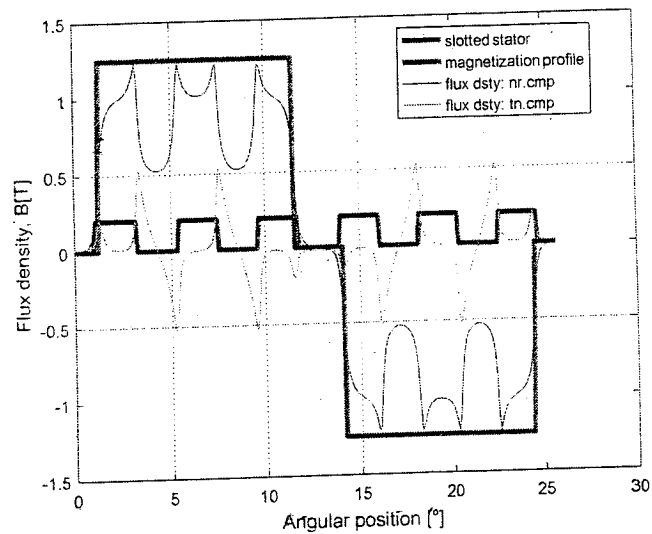
Figure 37, Airgap flux density produced by the permanent magnets

The angle zero is here defined to be at the middle of the first slot. As it can be seen, the magnetic field produced by the permanent magnets exhibits half wave symmetry with peak values along the teeth edges. The effect of armature slotting is very apparent by observing a drop of the magnetic potential for the normal component facing the slots. The level of the flux density is lower facing the slots. Similarly, the field tangential component drops to nearly zero facing the teeth. The assumption of infinitely permeable materials is thus satisfied.
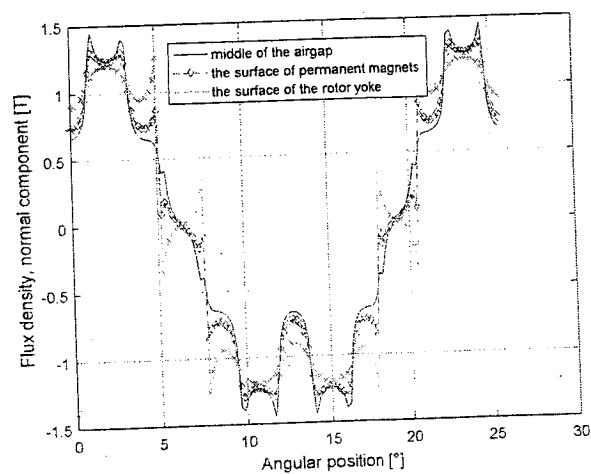
Figure 38, Flux density distribution in different regions of the machine

Figure 38 compares the distribution of the normal component of the magnetic field at different regions of the machine namely at middle of the airgap, at the surface of permanent magnets and at the surface of the rotor yoke. This graph clearly indicates that the influence of stator slots decays quickly with the distance for the stator core. The difference between the peak flux density for each case is also observed.

In order to illustrate the effect of the magnet shifting, figure 39 depicted the field distribution for the following parameters.

Magnet fraction, north (%)	85, 70, 65
magnet fraction, south (%)	75, 70, 70
magnet spacing, north (%)	50, 40, 45
magnet spacing, south (%)	50, 50, 35

Figure 39. Effect of magnetic shifting on the flux density distribution

The magnet shifting effect is apparent resulting in the difference between the two curves. This discrepancy leads to a lower cogging torque magnitude and has

negligible effect on the back-emf waveform. This will be described in the next chapter.

3.5. Cogging torque expression

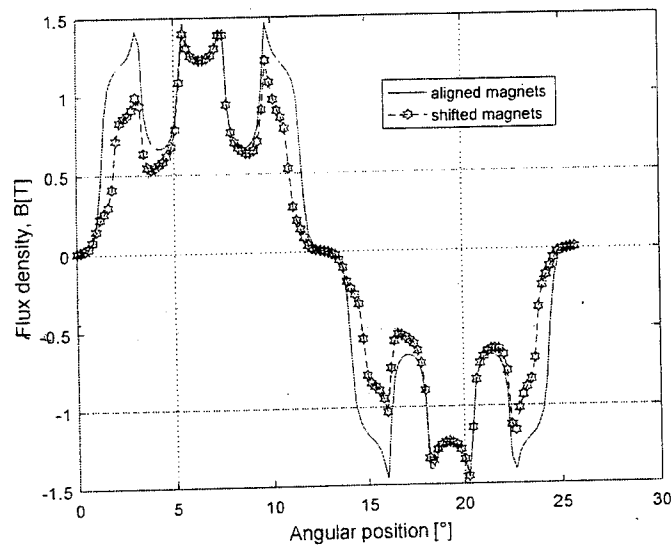Torque computation is performed using Maxwell stress tensor method applied at the interface region between the airgap and the PM magnets with null stator currents. The elementary force acting on one disc is given by $dF = \sigma_n ds + \sigma_t ds$. While the first component acts on the normal direction and can twist the discs, the second one is responsible for the torque production expressed in the following integral form over a closed as follows:

$$\Gamma = \iint_{(A_g)} r e_r \times dF = \iint_{(A_g)} (\mu_0 H_n H_t) r^2 dr d\varphi e_z$$

$$= \mu_0^{-1} \int_0^{2\pi} \int_{r_i}^{r_o} B_{\varphi|z=-g}^{(III,1)} B_{z|z=-g}^{(III,1)} d\varphi e_z \qquad (3.27)$$

A_g is the airgap cross-sectional area. Inserting the equations derived previously for the field solution and developing, the magnitude of the cogging torque is expressed by:

$$\Gamma_{cog} = \pi (3\mu_0)^{-1} \sum_{s=1}^{N_{sl}} (R_{o,s}^3 - R_{i,s}^3) \sum_{n \neq 0} \frac{\left(C_{n,s}^{(III,1)} E_n^{(M,1)} + E_{n,s}^{(III,1)} F_n^{(M,1)} \right) \cdot}{\left(sh(nz_0) - T_{n\lambda}(z_1) ch(nz_0) \right)} \qquad (3.28)$$

The dependency of the remanence Fourier coefficients and the airgap magnetic field coefficients is clearly illustrated in this expression. They are rotor position dependent. Therefore, equation (3.28) should be evaluated for every rotor angle position.

For disc-type machines, representing the machine by ten radial slices ($N_{sl} = 10$) is considered a good practice in order to predict the global quantities with an acceptable accuracy.

3.6. Induced voltage calculation

In order to compute the back-emf of a synchronous generator, we first determine the flux through the armature winding at a given angular position. Under no-load conditions, the magnetic flux produced by the magnets linking a pole pair for phase $'m'$ is given by:

$$\phi_g = \int_0^{\frac{2\pi}{N_p}} \int_{r_i}^{r_o} F_{d,m}(\varphi) B_{z|z=0}^{(II)} r \, dr \, d\varphi \qquad (3.29)$$

The winding distribution function $F_{d,m}$ shown in fig (3) carries information about the winding topology such as slot opening, coil span and location [19]. The corresponding Fourier series is expressed by:

$$F_{d,m}(\varphi) = a_0 + \sum_{n \neq 0} \begin{matrix} E_n^d \cos n \left(N_p \varphi - \dfrac{2(m-1)k\pi}{3} \right) + \\[2mm] F_n^d \sin n \left(N_p \varphi - \dfrac{2(m-1)k\pi}{3} \right) \end{matrix} \qquad (3.30)$$

The total flux per phase produced by the magnets is obtained by adding each elementary flux of all series-connected coils. Substituting (3.30) in (3.29) and developing, the flux becomes:

$$\begin{aligned} &\phi_{g,m} \\ &= \pi \frac{(r_o^2 - r_i^2)}{2} \sum_{k \neq 0} \begin{matrix} a_k^{(II)} \left(E_n^d \sin \dfrac{2(m-1)k\pi}{3} + F_n^d \cos \dfrac{2(m-1)k\pi}{3} \right) + \\[2mm] b_k^{(II)} \left(F_n^d \sin \dfrac{2(m-1)k\pi}{3} - E_n^d \cos \dfrac{2(m-1)k\pi}{3} \right) \end{matrix} \end{aligned} \qquad (3.31)$$

r_o and r_i are the outer radius and the inner radius of a given annular slice respectively. The back emf requires the flux calculation at the stator surface, i.e. $z = 0$. Moreover, if the axis of the coil is taken as reference, only the cosine terms in (3.30) exist and the flux expression is then reduced to:

$$\phi_{g,m} = \pi \frac{(r_o^2 - r_i^2)}{2} \sum_{k \neq 0} E_n^d \left(C_k^{(II)} \sin \frac{2(m-1)k\pi}{3} - E_k^{(II)} \cos \frac{2(m-1)k\pi}{3} \right) \tag{3.32}$$

The winding pitch factor and the slot opening factor are considered in the expression of the coefficient E_n^d [20]. The back emf for phase $'a'$ at a given rotational speed Ω is obtained by differentiating (3.32) with respect to time, i.e. $e_{ph} = {-d\phi}/{dt} =$

$-\Omega {d\phi}/{d\theta}$. This yields to the following expression:

$$e_{ph}(\theta) = -\Omega\pi(r_o^2 - r_i^2) \sum_{k \neq 0} E_k^d \frac{d}{d\theta} \left(E_k^{(III,1)} - E_k^{(M,1)} ch(kN_p g r_m^{-1}) \right) \tag{3.33}$$

The differentiation of the field coefficients with respect to the angular position for the back emf computation is carried out by solving the linear system:

$$\frac{dE_k^{(III,1)}}{d\theta} = (T_{\lambda p}(z_3)L)^{-1} \begin{bmatrix} (S_{k,01} + C_{k,01}L) \dfrac{dE_k^{(M,1)}}{d\theta} + \\ (S_{k,12} + C_{k,12}L) \dfrac{dE_k^{(M,2)}}{d\theta} + \\ \left(S_{k,20} + C_{k,2\frac{j\pi}{2}}L \right) \dfrac{dE_k^{(M,3)}}{d\theta} \end{bmatrix} \tag{3.34}$$

with

$$\frac{dE_k^{(M,\ell)}}{d\theta} = \frac{-(-1)^{(k)}}{k\pi} \begin{Bmatrix} B_{RN}^{(\ell)} \left(\cos kN_p \left(\theta_1^{(\ell)} + \theta_{mN}^{(\ell)} - \theta_0 \right) - \cos kN_p \left(\theta_1^{(\ell)} - \theta_0 \right) \right) \\ + \\ B_{RS}^{(\ell)} \left(\cos kN_p \left(\theta_2^{(\ell)} + \theta_{mS}^{(\ell)} + \theta_0 \right) - \cos kN_p \left(\theta_2^{(\ell)} + \theta_0 \right) \right) \end{Bmatrix}$$

3.7. Summary

No-load operation of PM synchronous axial flux generators is characterized by the induced voltage and the cogging torque. To compute these quantities, an electromagnetic based model has been derived in order to predict the exact airgap magnetic field distribution. Formulated in polar coordinates, this quasi-2D analytical model is derived from the application of Maxwell's equations for a multilayer surface

mounted permanent magnet generator where each magnet is subdivided into three pieces shifted in the normal direction. To this end, the machine is divided into three different regions and for each region the magnetic field is expressed in terms of Fourier series where the coefficients are determined by applying Neumann boundary conditions, continuous boundary conditions or a combination of both between regions. Furthermore, torque computation is performed using Maxwell stress tensor method applied at the interface region between the airgap and the PM magnets whereas the induced voltage per phase is obtained by means of the winding distribution function.

CHAPTER 4.

RESULTS AND DISCUSSION

4.1. Introduction

The analytical modeling of axial flux machines has been constantly developed since the advent of these machines and for different topologies. Usually, the cogging torque behavior in permanent magnet machines relies on the generalized forces theorem relating the torque to the system energy or coenergy variation with incremental rotor displacement. Another alternative relies on the field theory for which the torque is computed using Maxwell stress tensor that requires the calculation of the airgap magnetic field distribution in rotating machines. The main task of this work is to develop a 2D magnetostatic model to predict the airgap flux density with great accuracy by taking into account the slotting effect. As a by-product of this calculation, the cogging torque and the back-emf are computed with an acceptable level of accuracy compared to FEM analysis. The chief advantage of this semi-numerical analytical model is that it gives a starting point to the preliminary design and analysis of any electric machine. It offers a trade-off between the computational time and resources required by FEM based software and accuracy level. The most notable contributions of this work are:

- Development of an electromagnetic model for three-phase axial flux permanent synchronous machines using Maxwell's equations in magnetostatics. In this work, each surface mounted permanent magnet has been replaced by three pieces and shifted with respect to the interpolar axis as shown in figure 36.

- Computation of the cogging torque for a TORUS-S machine where the magnet shifting has proved to have a great impact on the peak amplitude reduction.

Computation of the back-emf. Simulation results show that shifting permanent magnets has little effect on the induced voltage waveform that becomes also more sinusoidal.

4.2. Parameters of the simulated axial flux machine

Table 6 presents the geometric dimensions and magnetic specifications for axial flux wind generator whose cross sectional area is shown in figure 36. No data are available for the stator and rotor iron cores because the magnetic materials are assumed highly permeable.

Table 6: Parameters of the simulated machine

number of slots	84	magnet fraction, north (%)	70, 60, 50
pole pairs	14		
Magnetization	parallel	magnet fraction, south (%)	70, 70, 60
outer radius (cm)	35		
inner radius (cm)	30	magnet spacing, north (%)	50, 25, 50
airgap length (mm)	1.5		
slot fraction (%)	50	magnet spacing, north (%)	50, 25, 50
PMs thickness (mm)	2/piece		

With these data, the number of slots per pole per phase is one. The magnetization was assumed to be parallel. Nevertheless, other types could be considered and each magnetization profile is characterized by the Fourier coefficients $E_k^{(M,\ell)}$ and $F_k^{(M,\ell)}$ that have a different impact on the airgap field distribution. The airgap length was set to 1.5mm which is typical for disc machines provided that discs are solidly attached to the mechanical shaft to avoid any deflection and avert the worst scenario case.

4.3. Numerical simulation results

In order to validate the proposed analytical model, the airgap flux density, the cogging torque, and the back-emf are checked using FEM. The FEM analysis is performed for the 2D configuration at the machine's mean radius under no-load conditions where a sketch of the line of forces is displayed in figure 40.
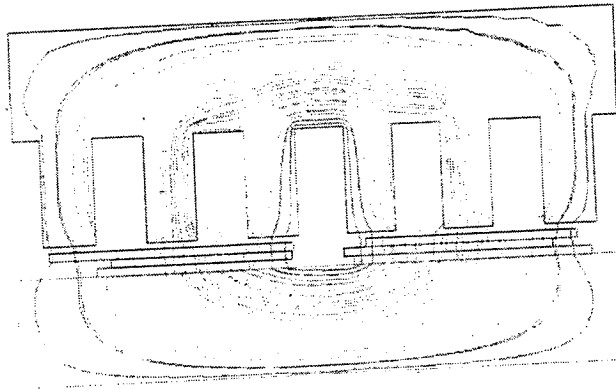

Figure 40. Illustration of the flux lines in one stage of the TORUS generator

As expected, the North Pole (on the left) drives the flux through the airgap into the stator teeth. The flux then travels circumferentially along the stator iron yoke and enters the rotor yoke through the opposite south pole (on the right) and takes the tangential path to join the north magnetic pole for closing the loop. It can also be seen that the magnetic materials are not saturated and slot leakage flux is negligible.

4.3.1. The airgap flux density distribution

A comparison of the predicted airgap flux density distribution calculated by the analytical approach and the FEM is shown in figure 41 for a slotted TORUS generator whose main parameters are given in table 6. The stator and rotor iron cores have been modeled by a natural Neumann boundary condition. Hence, the effect of magnetic saturation is neglected.
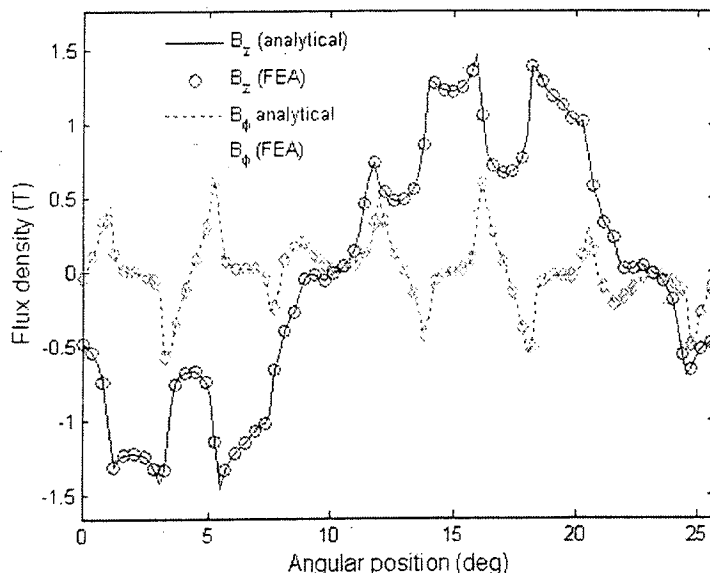
Figure 41. Comparison of the airgap flux density

By examining this figure, there is a good correlation between the analytically and

finite element predicted distributions of both the normal and the tangential airgap field

components evaluated at the machine's mean radius. Here, only one pole pair is

presented in the simulation because of periodicity considerations. This matching of

results is also good indicator that both back-emf and cogging torque can also be

predicted with a great accuracy using the proposed analytical approach. The slotting

effect is apparent and affects both the magnitude and the distribution of the airgap

flux density. This armature slotting effect is being accounted for when establishing

the boundary conditions between the airgap region and the slot openings as depicted

in equation (3.22). Figure 41 clearly shows that the normal component is reduced

facing the slot openings whereas the tangential component is almost zero under the

stator teeth area. It is worthy to note that the airgap flux density produced by the PM

has a zero average value over one period and a peak value of 1.5T in the airgap. This

level of flux density is acceptable for rotating machines and causes no saturation in teeth region or the stator yoke.

4.3.2. The cogging torque waveform

Among several design parameters that can affect directly the cogging torque fluctuation, the slots geometry (closed, semi-closed or open slots) is a major aspect studied by most designers. In fact because of the permeance variation in the slot opening the flux enters the teeth creating thus the cogging torque component. For radial type conventional machines, slots have parallel opening and as a results the cogging torque contribution remains the same along the axial direction and there is no need to decompose the machine into annular slices. While this is also true for axial flux machines, slots can have radial opening as shown in figure 42.
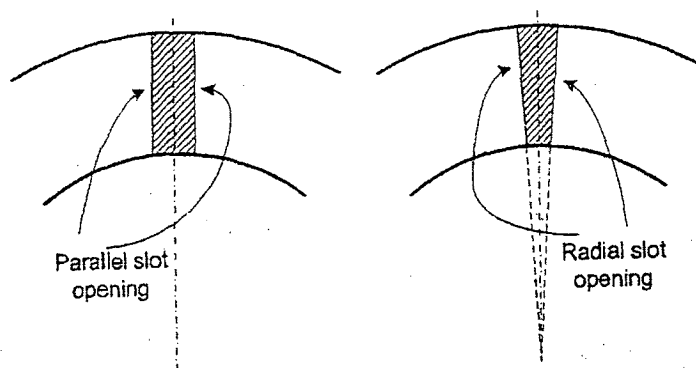

Figure 42. Parallel and radial slot openings for AFPM machines

When the slot openings are radial, the ratio of the width of the slot openings to the slot pitch is constant. As a result, to cogging torque contribution for each annular slice remains the same irrespective the radial position.

In this work, radial open slot openings and NdFeB parallel magnets are considered. The validation of the cogging torque waveform with respect to rotor position has been made against finite element predictions for the two cases: aligned magnets and shifted

magnets. Referring to figure 43, the analytical prediction fairly agrees with the finite element solution. This graph pertains to a double-rotor, single-stator TORUS-S machine whose parameters are given in table 6. In comparison with the FEM, the presented analytical method gives immediate results and allows for fast analysis of different geometries for permanent magnets.
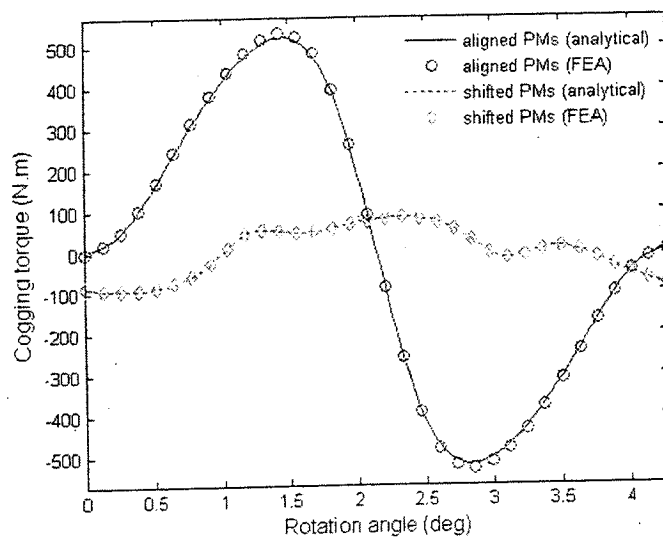

Figure 43, Cogging torque as affected by magnet shifting

For this configuration, each rotor disc interacting with the opposite slots generates 50% of the total cogging torque. This asymmetric disposition of permanent magnets resulting from shifting produces a cogging torque that peaks a very low values as shown in figure 43 where a peak reduction of 80% can be observed.

4.3.3. The back-emf waveform

The back-emf induced per turn due to the magnetic flux crossing the airgap is found by applying equation (3.33) where the winding factors are being taken into account expect the skewing factor which difficult to evaluate for axial flux machines especially for stator having parallel slot opening. The studied machine has 84 slots accommodating a three-phase single-layer drum-type winding as shown below.
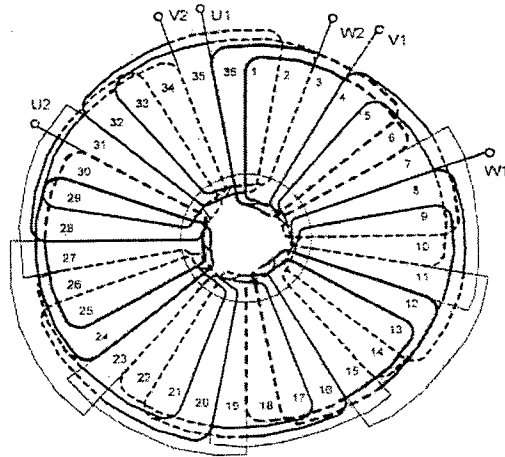
Figure 44. single-layer toroidal winding of AFPM machines

A comparison of the back-emf waveform against those obtained with the FEM is displayed in figure 45 in this is for both cases: aligned magnets and shifting magnets. A perfect agreement between the analytical predicted model and the FEM results is achieved.
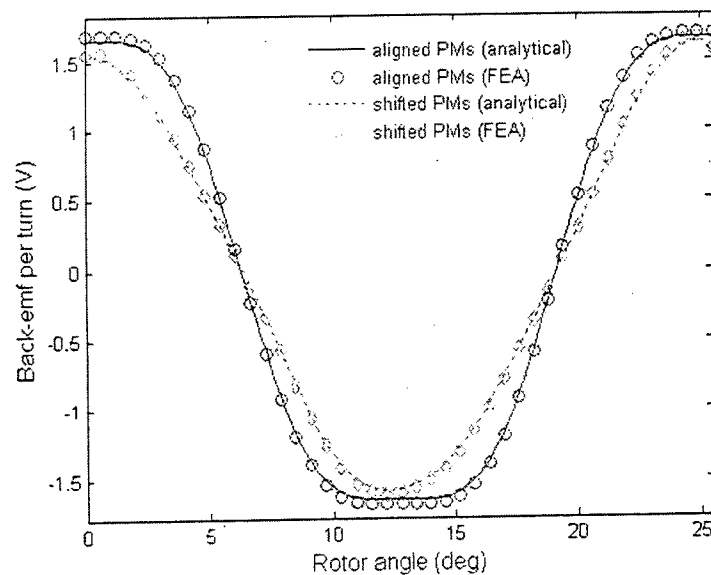

Figure 45. Back-emf waveform at 230 rpm

Also, it can be easily seen that the induced voltage magnitude is not only unaffected by the permanent magnet shifting but the waveform becomes more sinusoidal resulting in less harmonic content and better electrical performance of the wind generator.

4.4. Summary

This chapter has provided a comparison between the analytically predicted quantities from the proposed model and the corresponding results from FEM is made. Results show that the flux density waveform and the cogging torque and the back-emf variations are in good agreement. The simulation is made for a TORUS-S machine having radial slot openings and parallel magnets. Because of its accuracy, this developed model can be applied to other configurations and different winding topologies.

General conclusion

A quasi-2D analytical model formulated in polar coordinates based on Maxwell's equations has been derived for a multilayer surface mounted permanent magnet wind generator where each magnet is subdivided into three pieces shifted in the normal direction. This approach involves the solution of the Laplace/quasi-Poissonian field equations. In comparison with the finite-element method (FEM), the presented analytical method gives immediate results and allows for fast analysis. It also caters for both internal and external machines and requires by far less computational time and resources than the FEM. The magnetic field distribution, the cogging torque, and the back-emf waveforms all show an excellent agreement with those obtained from FEM. Simulation results show that stacking and shifting magnets in the normal direction will not only reduce the cogging torque to a low level but also improves the back-emf waveform without any considerable loss of magnitude. Therefore, it is suitable during the initial pre-design stage of wind turbine generating systems where the cogging torque is a major start-up concern at low wind speed.

References

[1] "Annual energy outlook 2017, with projections to 2050," *US Energy Information Administration 2017.*

[2] "Global trends in renewable energy investment 2017," *United Nations Environment Program, FS-UNEP 2017.*

[3] "Renewable energy policy framework for the 21st century," *REN21, http://www.ren21.net.*

[4] G. Son, H. Lee, "Estimation of wind turbine rotor power coefficient using RMP model," *IEEE Industry Applications Society Annual Meeting, Houston TX 2009.*

[5] T. Ackermann, "Wind power in power systems," *John Wiley,* 2005.

[6] A. Kumari, S. Marwaha and A. Marwaha, "Comparison of methods of minimization of cogging torque in wind generators using FE analysis," *Journal of the Indian institute of science,* vol. 86, pp. 355–362, 2006.

[7] N. Min-Fu and Y. Yu-Han, "Rotor eccentricity effect on cogging torque of PM generators for small wind turbines," *IEEE transaction on Magnetics,* vol. 49, pp. 1897–1900, 2013.

[8] E. Muljadi and J. Green, "Cogging torque reduction in a permanent magnet wind turbine generator," *in Proceedings of 21st American Society of Mechanical Engineers Wind Energy Symposium,* Nevada, January 2002.

[9] M. Lukaniszyn and A. Mlot, "Analysis of a BLDC motor with fractional slot winding," *in Proceedings of Electrotechnical institute, technical university of Opole,* vol. 229, pp. 115–125, 2006.

[10] J. Sopanen, V. Ruuskanen, V., Nerg and J. Pyrhönen, "Dynamic torque analysis of a wind turbine drive train including a direct-driven permanent-magnet generator," *IEEE transaction on industrial electronics,* vol. 58, pp. 3859–3867, 2011.

[11] T. Zou, D. Li and R. Qu, "Analysis of dual-rotor, toroidal winding axial flux Vernier permanent magnet machine," *IEEE transactions on industry application,* vol. 53, pp. 1920–1930, 2017.

[12] S. Kahourzade, A. Mahmoudi and H. Ping, "A comprehensive review of axial flux permanent magnet machines," *Canadian Journal of Electrical and Computer Engineering,* vol. 37, pp. 19–33, 2014.

[13] H. Qingling and W. Qunjing, "Design techniques for reducing cogging torque in low-speed permanent magnet wind power generator," *Int. Conf. on Electrical Machines and Systems*, China, pp. 1–3, 2011.

[14] S. Zhu, Z. Jiang, Z. Zhu and C. C. Chan, "Analytical methods for minimizing cogging torque in permanent-magnet machines," *IEEE Transactions on Magnetics*, vol. 45, pp. 2023–2031, 2009.

[15] V. Sempere, M.B. Payán, and J.C. Bueno, "Cogging Torque Cancellation by Magnet Shaping in surface mounted permanent magnet motors," *IEEE Transactions on Magnetics*, vol. 53, no. 7, 2017.

[16] Y. Ueda, H. Takahashi, A. Ogawa, T. Akiba and M. Yoshida, "Cogging-Torque Reduction of Transverse-Flux Motor by Skewing Stator Poles", *IEEE Transactions on Magnetics*, vol. 52, 2016.

[17] W. Ren and Q. Xu, "A novel technique of cogging torque reduction in mass-produced surface mounted permanent magnet motor using tooth notching pairing," *IEEE International Magnetics Conference*, July 2015.

[18] L. Xiao, J. Li and R. Qu, "Cogging torque analysis and minimization of axial flux PM machines with combined rectangle shaped magnet," *IEEE transaction on industry applications*, vol. 53, pp. 1018–1027, 2017.

[19] J. Wanjiku, M. Khan; P. Barendse, "Influence of slot opening and tooth profile on cogging torque in axial flux PM machines," *IEEE transaction on industrial electronics*, vol. 62, pp. 7578–7589, 2015.

[20] C. Xia, Z. Chen, and T. Shi, "Cogging torque modeling and analyzing surface mounted permanent magnet with auxiliary slots," IEEE transactions on magnetics, vol. 49, pp. 5112–5123, 2013.

[21] T. Lubin, S. Mezani, A. Rezzoug, "2D exact analytical modeling for surface mounted permanent magnet motors with semi-closed slots," *IEEE transactions on magnetics*, vol. 47, pp. 479–492, 2011.

[22] R. Sprangers, J. Paulides and B. Gysen, "Magnetic saturation in semi analytical harmonic modeling for electric machines analysis," *IEEE transactions on magnetics*, vol. 52, 2016.

[23] S. Boroujeni, A. mohammadi and A. oraee, "Approach for analytical modeling of axial flux PM machines," *IET electric power and applications*, vol. 10, pp. 441–450, 2016.

[24] H. Tiegna, A. Bellara, Y. Amara, and G. Barakat, "Analytical modeling of the open-circuit magnetic field in axial flux permanent-magnet machines with semi-closed slots," *IEEE transactions on magnetics*, vol. 48, pp.1212–1226, 2012.

[25] B. Gysen, K. Meesen and J. Paulides, "General formulation of the electromagnetic field distribution in machines and devices using Fourier analysis," *IEEE transactions on magnetics*, vol. 26, pp.39–52, 2009.